LAWRENCE
LIVERMORE
NATIONAL
LABORATORY

LLNL-JRNL-404785

Reshocks, rarefactions, and the generalized Layzer model for hydrodynamic instabilities

K. O. Mikaelian

June 19, 2008

Physics of Fluids

Disclaimer

Reshocks, rarefactions, and the generalized Layzer model for hydrodynamic instabilities

Karnig O. Mikaelian
Lawrence Livermore National Laboratory
Livermore, California 94551

Abstract

We report numerical simulations and analytic modeling of shock tube experiments on Rayleigh-Taylor and Richtmyer-Meshkov instabilities. We examine single interfaces of the type A/B where the incident shock is initiated in A and the transmitted shock proceeds into B. Examples are He/air and air/He. In addition, we study finite-thickness or double-interface A/B/A configurations like air/SF_6/air gas-curtain experiments. We first consider conventional shock tubes that have a "fixed" boundary: A solid endwall which reflects the transmitted shock and reshocks the interface(s). Then we focus on new experiments with a "free" boundary—a membrane disrupted mechanically or by the transmitted shock, sending back a rarefaction towards the interface(s). Complex acceleration histories are achieved, relevant for Inertial Confinement Fusion implosions. We compare our simulation results with a generalized Layzer model for two fluids with time-dependent densities, and derive a new freeze-out condition whereby accelerating and compressive forces cancel each other out. Except for the recently reported failures of the Layzer model, the generalized Layzer model and hydrocode simulations for reshocks and rarefactions agree well with each other, and remain to be verified experimentally.

I. Introduction and Motivation

Hydrodynamic instabilities play a major role in natural phenomena such as supernova explosions[1] and in man-made devices such as Inertial Confinement Fusion (ICF) capsules[2]. In particular, the Rayleigh-Taylor[3] (RT) and Richtmyer-Meshkov[4] (RM) instabilities, associated with accelerating and shocked interfaces respectively, lead to the eventual turbulent mixing of the fluids. Perturbations at the interface of amplitude η and wavelength λ start in the linear regime ($\eta k << 1$, where $k = 2\pi/\lambda$), proceed to the nonlinear regime ($\eta k \sim$1-2), and finally enter a turbulent regime where multiple wavelengths emerge. All three regimes are presently under extensive study theoretically, numerically, and experimentally[5].

Most of the studies on RT and RM instabilities have naturally focused on single interfaces undergoing a constant acceleration or a shock to bring out the essential or "classical" behavior of these instabilities. Multiple interfaces leading to multiple waves are present in the actual applications. In a supernova explosion a strong shock from the dense center moves out through successively less dense layers before emerging into the interstellar medium. At each crossing from a heavy to a lighter medium a rarefaction is generated moving back towards the center and rarefying the previously shocked interface. Similarly in ICF implosions: A strong shock moves inwards through successively lighter fluids generating rarefactions. For double-shell capsules[6], the shock strikes a heavy shell which generates a reflected shock. In all cases the shock reaching the center reflects on itself and reshocks the imploding shell. Such implosions/explosions lead to a complex evolution of perturbations at multiple interfaces. The main purpose of this paper is to show that shock tubes, with minor modifications, can be used to study the effect of multiple waves and/or interfaces. Since perturbations evolve into the nonlinear

regime we believe the best way to demonstrate this capability, short of doing the experiments, is to present numerical simulations of realistic future experiments. We also present an analytic model for the nonlinear regime based on the pioneering work of Layzer[7] and its recent extensions[8,9,10,11]. Since many of the proposed experiments involve fluids with changing densities, an extension of the standard Layzer model is called for. We develop such a Generalized Layzer model (GLM) and compare it with simulations.

Using a linear, incompressible theory, a first look into the effect of multiple shocks revealed[12] a rich variety of possible outcomes—some 15 cases (see Fig. 3 in Ref. 12). A straightforward extension of Richtmyer's model, often called the "impulsive model", leads to[12]:

$$\dot{\eta}_+ = \dot{\eta}_- + \Delta v k A \eta_s \qquad (1)$$

where $\dot{\eta}_+$ is the growth rate after the second shock, $\dot{\eta}_-$ is the growth rate before that second shock (and possibly induced by a first shock), Δv is the jump in velocity induced by the second shock, A is the Atwood number,

$$A = \frac{\rho_B - \rho_A}{\rho_B + \rho_A}, \qquad (2)$$

where $\rho_{A,B}$ are the densities of the two fluids, and η_s is the amplitude of the perturbation at the time the second shock strikes the interface. Let us recall two special cases that can be inferred from Eq. (1). The first occurs when the first term on the right-hand-side of Eq. (1) is positive and the second term is negative (or vice versa): It is then possible for these two terms to cancel each other out leading to "freeze-out", i.e., $\dot{\eta}_+ = 0$. The second case worth noting is that if $\eta_s = 0$ then $\dot{\eta}_+ = \dot{\eta}_-$ (Fig. 3i in Ref. 12) meaning that the second shock has no effect on the growth rate. An example will be given later in this paper. As to freeze-out, a recent analysis[13] shows that the idea of a second shock canceling the effect of the first shock is valid, provided that nonlinear

modifications to Eq. (1) are taken into account[13]. All these predictions remain theoretical/numerical and have no experimental verification.

Figure 1 shows a generic shock tube and some of our notation. The first shock, if there is one, moves "down" in a semi-infinite fluid A towards fluid B, often called the "test gas", shocking the interface between the two fluids having perturbations of wavelength λ and initial amplitude η_0. A shock is transmitted into fluid B.

What happens to that transmitted shock depends on the second boundary of fluid B (the first boundary being the A/B interface). In all experiments and, we believe, all simulations performed to date that "bottom" boundary has been a solid wall, in which case the shock is reflected back up and reshocks the A/B interface. Another alternative that we consider in this paper is to have a membrane as the bottom boundary that disintegrates either mechanically or upon the arrival of that transmitted shock sending a *rarefaction* up towards the A/B interface[14]. Thus, depending on the nature of that bottom boundary, the second wave seen by the A/B interface may be a shock or a rarefaction.

With two waves, one can have shock/reshock, the case most commonly studied so far with a solid endwall. Alternatively, replacing the end wall with a membrane we have shock/rarefaction or rarefaction/shock, the latter carried out by opening the bottom membrane first and allowing the rarefaction to reach the interface *before* the shock hits it. With a simple shock tube as in Fig. 1 it is clear that the second wave always moves in a direction opposite the first wave. A more complex shock tube having two consecutive firing chambers is needed to produce two co-propagating waves.

We limit ourselves to the following three systems: He/air, air/He, and air/SF_6/air. The first and last systems have already been studied for shock/reshock so we concentrate only on the

effect of a rarefaction. The air/He system (A = air, B = He) is relevant to both supernovae and ICF as representative of heavy-to-light shock propagation and, as we will find out, oscillatory behavior under rarefaction. We should note that air and He are used here as representatives: Heavy and light gases with similar density ratios are expected to behave the same way (air/SF_6 is a good substitute, for example, for He/air). There are subtle compressibility effects invalidating Richtmyer's impulsive model and his prescription for compressibility[15] but none of them affect our results on high (~7) density contrasts and low (~1.2) Mach numbers.

In Section II we consider shock/reshock of the air/He system. In Section III we consider the effect of a rarefaction on all 3 systems. In Section IV we consider shock/rarefaction, and in Section V we simulate the more demanding rarefaction/shock experiments with emphasis on the *timing* between the rarefaction and the shock. Conclusions and future work are discussed in Section VI. The analytic GLM is presented in the Appendix; it is used in Sections III and IV to compare with numerical simulations, all carried out with the two-dimensional hydrocode CALE[16].

II. Shock/Reshock

We have already presented[17] calculations on shock and reshock of the air/SF_6/air system, often called gas-curtain experiments[18]. So far only shocks have been produced experimentally, but preparations are in progress to capture the effect of reshocks.[19]

Similarly for the He/air system: our calculations are given in References 20 and 21 and compared with a Layzer-type analytic model. Therefore, we consider only the air/He system in this Section.

Air/He

A Mach 1.2 shock proceeds from air (fluid A in Fig. 1) towards He (fluid B), striking the interface at $t=0$. The shock tube is 26 cm wide with two sinusoidal perturbations of $\lambda=13$ cm across the interface, as in earlier work[20,21] on He/air. The main difference here is that the evolution of the perturbation starts with a phase reversal and grows thereafter. The length of the shock tube is again 122 cm; however, the transmitted shock travels faster in this case and, reflecting off the solid endwall, returns to reshock the interface at 2 ms (compared with 4.2 ms for the He/air case). Snapshots of the air/He interface starting with $\eta_0 = 0.7$ cm are shown in Fig. 2, to be compared with the He/air case (Fig. 5 of Ref. 20).

The bubble amplitude $\eta(t)$ as calculated by CALE is shown in Fig. 3 for $\eta_0 =$ 0.35 and 0.7 cm, showing a phase reversal upon shock but none at reshock (the opposite happens for the He/air case). To compare with a Layzer-type model[7] we write the solution found earlier (Eq. (10) of Ref. 8) in the following manner:

$$\eta(t) = \eta_0 + \frac{1}{k_L}\ln(1+\dot{\eta}_0 k_L t) \tag{3}$$

where k_L is defined by

$$\dot{\eta}(t\to\infty) \equiv \dot{\eta}_\infty = \frac{1}{k_L t}. \tag{4}$$

Although Eq. (3) was derived for special values of η_0 (there were no constraints on $\dot{\eta}_0$), it is clearly self-consistent for arbitrary values of η_0, $\dot{\eta}_0$, and $\dot{\eta}_\infty$. It will be seen as a special case of the GLM in the Appendix. Of course, the origin of time is also arbitrary and t can be replaced by $t-t_0$ as long as $\eta(t)=\eta_0$ and $\dot{\eta}(t)=\dot{\eta}_0$ at $t=t_0$.

We will apply Eq. (3) starting at $t = t_0 = 0.2$ ms when the amplitude goes through zero, i.e. start with $\eta_0 = 0$. A similar approach was taken recently[22] when the amplitude undergoes a phase reversal. To calculate $\dot{\eta}_0$ we use the impulsive model as modified by Meyer and Blewett[23] or, more recently, by Vandenboomgaerde *et al*[24]. According to Meyer and Blewett[23]

$$\dot{\eta}_0 = \frac{1}{2}(\eta_{0-} + \eta_{0+}) A_{after} \Delta v k \tag{5a}$$

where $\eta_{0-}(\eta_{0+})$ is the amplitude before (after) shock arrival and A_{after} is the Atwood number after shock arrival. According to Vandenboomgaerde *et al*[24]:

$$\dot{\eta}_0 = \frac{1}{2}(\eta_{0-} A_{before} + \eta_{0+} A_{after}) \Delta v k \tag{5b}$$

with obvious notation. Equations (5a) and (5b) yield essentially the same result because $A_{after} / A_{before} = 0.763 / 0.757 \approx 1.008$. As noted by Richtmyer, η_{0-} and η_{0+}, the amplitudes before and after the shock, are related by

$$\eta_{0+} = (1 - \Delta v / W_i) \eta_{0-} \tag{6}$$

where Δv is the jump velocity of the interface, 14.9 cm/ms, and W_i is the incident shock speed, 41.2 cm/ms. The factor $(1 - \Delta v / W_i)$ is often referred to as the compression factor, and is about 0.64 in the present case (air/He at Mach 1.2). Using $k = 2\pi / 13$ cm^{-1}, we obtain $\dot{\eta}_0 = 1.57$ cm/ms and 3.15 cm/ms for $\eta_{0-} = 0.35$ cm and 0.70 cm respectively.

The last variable needed in Eq. (3) is k_L, defined via the asymptotic bubble velocity $\dot{\eta}_\infty$ in Eq. (4). For $A = 1$, $k_L = 3k/2$ (see Ref. 8). For arbitrary A, we compare Eq. (4) with the asymptotic bubble velocity given in Ref. 10 and find

$$k_L = \frac{3(1 + A)k}{3 + A}. \tag{7}$$

A more general expression covering arbitrary A and 2D or 3D geometry is given in the Appendix (Eq. A26a). Since $A = A_{after} = 0.763$, we obtain $k_L = 1.4k \approx$ 0.68 cm^{-1} for $\lambda = 13$ cm.

The continuous lines in Fig. 3 show the results of using Eq. (3) with the above values of η_0, $\dot{\eta}_0$, and k_L. As in the He/air case[20] we see that the Layzer model is a good description of the bubble amplitude in the nonlinear regime.

The evolution of $\eta(t)$ in Fig. 3 is consistent with the observation[8] that the initial amplitude η_0 affects only the initial growth rate $\dot{\eta}_0$ and not the late-time bubble velocity $1/k_L t$.

III. Rarefaction

As far as we know, pure rarefaction experiments have not been considered previously although they are, we believe, easier to perform—no shock is involved (combination of shocks and rarefactions are treated in Sections IV and V). Referring to Fig. 1, we consider the case with no shock. Instead, the membrane at the bottom of that figure is removed at a certain (negative) time sending a rarefaction up to collide with the interface or gas-curtain. In analogy with the shock case, we take t = 0 as the collision time, after which the interface(s) move down and the perturbations evolve. For simplicity we assume that the lower membrane separates gas B at atmospheric pressure from vacuum, so that upon removal (at $t = -d/c_B$, c_B = sound speed of gas B and d =distance between the membrane and the interface) gas B exhausts into a vacuum channel.

From a theoretical point of view we find it more challenging to describe how perturbations evolve at interfaces subjected to a rarefaction, as opposed to a shock. There are two reasons: First, the interface does not move at a constant average velocity, as it does in a shock. Second, the fluids on either side of the interface continue to decompress with time, in contrast to

the shock case where the densities change instantaneously but remain at their new values after the passage of the shock. We will present direct numerical simulations of all three systems He/air, air/He, and air/SF_6/air, and compare the numerical results with the Generalized Layzer Model.

A. He/air

The calculation is initiated with a "free" boundary condition at the lower edge of the problem (see Fig. 1) and the time is set to -3.5 ms (d = 122 cm, c_{air} = 34.8 cm/ms). Before we discuss the evolution of perturbations at the He/air interface we show in Fig. 4 the average or one-dimensional behavior of the interface acceleration and the densities ρ_A and ρ_B (A = He, B = air) near the interface as functions of time for $t > 0$. Note that $\rho_A(t)/\rho_A(0)$ and $\rho_B(t)/\rho_B(0)$ have similar but not identical dependence on time because the adiabatic indices are different (we have used γ_{He} = 5/3 and γ_{air} = 1.4). The acceleration is clearly not a delta-function of time as it would be for a shock.

Despite these differences the effect of a rarefaction moving up is, in very broad terms, similar to the effect of a shock moving down. In Fig. 5 we display the He/air interface with initial perturbations of $\lambda = 13$ cm and $\eta_0 = 0.7$ cm, in direct comparison with the shock case (Fig. 5 of Ref. 20): In both cases the perturbation grows with no phase change. The gross features are the same: mushrooming spikes and round bubbles. To compare the shock and the rarefaction cases, however, one must adapt a common metric and we propose this to be the average distance traveled by the interface. Thus we compare the interfaces after both have traveled say ~50 cm (t ~3.0 ms for a shock, ~3.4 ms for a rarefaction) and find that there is substantially more perturbation growth in the case of a rarefaction (by about a factor of 2), due in part to the fact that the gases decompress (by about a factor of 1.4) under rarefaction. As we will see below, the

time evolution of the bubble amplitude is quite different here: Whereas $\eta(t)$ grows only logarithmically in the case of a shock (see Eq. (3) above or Fig. 6 in Ref. 20), it grows linearly for the case of a rarefaction. Before we display $\eta(t)$, however, we ask if there is an analytic model that can describe it. As far as we know such a model has not been developed previously, and for that purpose we present the GLM in the Appendix. The new elements are displayed in Fig. 4: $g(t)$ and $\rho_{A,B}(t)$. For RT and RM instabilities, $g(t) = const.$ and $g(t) \sim \delta(t)$ respectively, while for rarefactions $g(t)$ decays with time.

In addition to the time-dependence of $g(t)$, the new element is the time-dependence of the densities $\rho_{A,B}(t)$. The closest model was developed by Goncharov and Li[11] for a single fluid with a time-dependent density. The GLM is a two-fluid Layzer model with arbitrary $\rho_{A,B}(t)$.

To calculate $\eta(t)$ analytically one must solve the following two coupled nonlinear but ordinary differential equations:

$$\frac{d}{dt}(\rho_B \eta_2) = -\frac{ck}{4}\left[k + \frac{4(1+c)}{c}\eta_2\right]\frac{d}{dt}(\rho_B \eta) \quad , \tag{8}$$

and

$$\begin{aligned} &\rho_B\left\{\frac{ck}{4}\frac{d}{dt}\left[\frac{1}{\rho_B}\frac{d}{dt}(\rho_B\eta)\right] + \frac{c^2k^2}{8}\left[\frac{1}{\rho_B}\frac{d}{dt}(\rho_B\eta)\right]^2\right\} \\ &+\rho_A\left\{\frac{ck}{4}\dot{b}_1 - \frac{c^2k^2}{8}b_1^2\right\} + (\rho_B - \rho_A)(g + \ddot{\eta})\eta_2 = 0, \end{aligned} \tag{9}$$

where

$$b_1 \equiv \frac{\frac{1}{k\rho_A}\frac{d}{dt}(\rho_A \eta_2)}{(1+c)\eta_2 - \frac{ck}{4}}. \tag{10}$$

Eqs. (8) and (9) must be solved for the two unknowns $\eta(t)$ and $\eta_2(t)$, all other quantities like $\rho_A(t)$, $\rho_B(t)$, $g(t)$ being "given" as input. The constant c is determined by the geometry of the flow: $c = 2$ for planar perturbations, often called curtain-like or 2D, in which case $k = 2\pi/\lambda$ with λ = wavelength of the perturbations, i.e., the interface at $t = 0$ is given by $\eta_0 \cos(kx)$. For tubular flow, often called "pipe-flow" or 3D axisymmetric flow, $c = 1$ and $k = \beta_n / R$ where β_n is a zero of J_1, the Bessel function of order one, R is the radius of the pipe, and the interface at $t = 0$ is given by $\eta_0 J_0(kr)$. All our simulations are 2D hence we set $c = 2$ and $k = 2\pi/13$ cm^{-1}.

We refer to Eqs. (8) and (9) as the GLM equations. As usual, we denote a time derivative by an overdot, hence $\ddot{\eta} \equiv d^2\eta/dt^2$. Eqs (8) and (9) are first order and second order respectively, and therefore we need three initial conditions: $\eta(0) \equiv \eta_0$, $\dot{\eta}(0)$, and $\eta_2(0)$. We take $\dot{\eta}(0) = 0$. As for η_2, it is related to the curvature of the interface (see the Appendix) and is the coefficient of the second-order term in a Taylor expansion of the interface near $x = 0$ or $r = 0$. Expanding $\cos(kx)$ or $J_0(kr)$, we get $\eta_2(0) = -ck^2\eta_0/4$. Consequently, we have only one free parameter, the initial amplitude η_0.

In Fig. 6, we display the CALE and the GLM results for the $\eta_0 = 0.7$ cm case (snapshots in Fig. 5). We see good agreement, with GLM underestimating the amplitude by 7–8% at late times. Although the acceleration is not constant in time (see Fig. 4) the amplitude grows linearly with time in the late nonlinear regime reminiscent of RT growth. It is important to use the time-dependent $g(t)$ and $\rho_{A,B}(t)$ to obtain such good agreement.

In the linear regime ηk << 1 the GLM reduces to a single simple equation

$$\rho_B \frac{d}{dt}[\frac{1}{\rho_B}\frac{d}{dt}(\rho_B\eta)] + \rho_A \frac{d}{dt}[\frac{1}{\rho_A}\frac{d}{dt}(\rho_A\eta)] - (\rho_B - \rho_A)gk\eta = 0 \qquad (11)$$

with $\eta_2(t) = -ck^2\eta(t)/4$. Eq. (11) reduces to Rayleigh's equation, $\ddot{\eta} - gkA\eta = 0$, for constant $\rho_{A,B}$ with the Atwood number A as defined in Eq. (2).

As a check, we simulated the same He/air rarefaction system with $\eta_0 = 0.05$ cm. In Fig. 7, we compare the three results: CALE, GLM, and linear. Clearly, the linear approximation, Eq. (11), greatly overestimates the perturbation once it enters the nonlinear regime, $\eta > 1$ cm. CALE and the GLM show good agreement in the nonlinear regime and agree with the linear result for small η.

B. Air/He

We now interchange the gases air $\leftrightarrow$ He and let the rarefaction move up through the He and reach the air/He interface. This takes about 1.2 ms since c_{He}=101 cm/ms. The interface acceleration and the densities are shown in Fig. 8. Compared with Fig. 4, the acceleration of the interface and the decompression of the gases are larger here, approximately by a factor of ~3.

The critical difference, however, is that it is now a heavier gas (air) accelerating a lighter gas (He). This is well known to be a stable configuration, and indeed the perturbations are found to oscillate with time and amplify in response to the decompression of the gases. Snapshots of the air/He interface for λ=13 cm and $\eta_0 = 0.7$ cm are shown in Fig. 9, to be compared with the He/air case of Fig. 5. The amplitude goes thru zero at ~0.6 ms and also at $t \approx 2$ ms. The bubble amplitude calculated by CALE (dashed curve) is shown in Fig. 10 as a function of time.

In the same figure, we show $\eta(t)$ calculated by the GLM, Eqs. (8–9). It fails miserably. This is the first portrayal, we believe, of the failure of Layzer's model on such a massive scale: It

predicts uniform growth after a phase change, instead of amplified oscillations. Needless to say, this assertion is based on the tacit assumption that CALE calculations are correct—we hope other calculations and eventual experiments will confirm this claim.

The reader might surmise that the original Layzer model with *constant* densities also fails for the stable case, i.e., $gA < 0$, and indeed this is true, as reported recently[25]. We emphasize that this failure occurs for the *nonlinear* model only - the linear model, Eq. (11), is valid for *any* $g(t)$. Since the nonlinear model does reduce to the linear model for small η, we expect and find good agreement for very small η_0. To illustrate, in Fig. 11 we compare the linear and nonlinear results and a CALE calculation with $\eta_0 = 0.05$ cm. All three indicate oscillations with time, as expected. Unlike the He/air case (Fig. 7) where the linear theory greatly overestimated η(t), here the linear theory is as good if not a better match to the CALE results than the nonlinear GLM, though the differences are small at such small amplitudes.

We have no alternative nonlinear theory to offer at this time. As discussed in the Appendix and Ref. 25, the failure is not associated with having time-dependent accelerations or densities and occurs with the "classical" Layzer model, meaning constant densities and accelerations. For stable situations, therefore, we recommend using the linear theory, Eq. (11), simply because it is "less wrong" than the GLM. For example, using Eq. (11) for the case shown in Fig. 10 with $\eta_0 = 0.7$ cm, we would have had errors of "only" ~30% instead of the completely erroneous GLM result. In Fig. 12, we compare CALE, GLM, and linear theory for $\eta_0 = 0.35$ cm. Although one may balk at using linear theory when $\eta_0 k \approx 0.17$, it is clearly a much better match to CALE than the nonlinear GLM.

One might argue that when η changes sign $\eta^{bubble} \rightarrow \eta^{spike}$ for which a different set of equations must be used.[10] From Figs. 10 and 12 (and Fig. 19 below) we note that the model fails *before* $\eta(t)$ crosses zero. In addition, we have found[25] that that model for spikes is deficient even for the more standard applications of the Layzer model (constant densities and accelerations) and, at present, can offer no remedy other than the linear result for stable accelerations.

The above failure of the GLM is distinct and separate from another failure that occurs even for *unstable* accelerations where Layzer's model has been traditionally applied. That failure, associated with large η_0, is discussed in Ref. 25 and in the Appendix also.

C. Gas-curtain: air/SF6/air

In these experiments[18] a perturbed SF_6 gas layer sandwiched between air on both sides is subjected to a Mach 1.2 shock. Here we replace that shock by a rarefaction.

Our CALE simulations[17] showed good agreement with the single-shock experiments[18] and made predictions, yet to be verified, about the effect of a reshock coming from a solid endwall 15 cm away. For brevity we shall consider the same system here, and refer to Ref. 17 as to how the perturbations in the gas-curtain are set up, etc. The only change is replacing the solid endwall by a membrane that is burst at $t = -0.43$ ms. A rarefaction moves "up" through the air and reaches the SF_6 layer at t = 0. The subsequent evolution is shown in Fig. 13.

The ubiquitous bubble-and-spike structure, which appears here as well as in the shock case, is stretched along the direction of the flow because of the decompression of the SF_6 curtain. The shock experiments have been used by various researchers as a vehicle for hydrocode validation,[26] and we believe future rarefaction experiments will provide equally, if not more, challenging data as displayed in Fig. 13, to be compared with the shock case (Fig. 10 in Ref. 17).

As to analytic modeling, the GLM must be considerably expanded to include finite-thickness and spatial density gradient effects before it can be applied to gas-curtain experiments, be they shock or rarefaction driven. Linear theory with sharp interfaces gives qualitative agreement[27] with the experiments (sinuous, upstream mushrooms, and downstream mushrooms[18]), but only full hydrocode simulations can capture the detailed shapes and density fields that arise when a perturbed gas-curtain is shocked or rarefied.

IV. Shock/Rarefaction

We have studied how each of the three systems (He/air, air/He, air/SF_6/air) respond to a single shock, a single rarefaction, or a shock followed by reshock, the reshock coming naturally from the solid endwall of the tube (Fig. 1) situated 122 cm away in the He/air and air/He cases, and 15 cm away in the gas-curtain case. Clearly, there are two more double-wave combinations that these systems can be subjected to, both involving the replacement of the solid endwall by a membrane: shock/rarefaction and rarefaction/shock. The first combination is studied in this section, the second in Sec. V.

The shock/rarefaction set up is identical to the shock/reshock set up with the above mentioned replacement. Therefore the evolution of all three systems is the same as before until the arrival of the second wave. As the transmitted shock approaches the end of the tube, the membrane bursts and thus a rarefaction, instead of a shock, moves "up" to meet the downward moving shocked interface or gas-curtain. Let us consider what happens in each system.

A. He/air

In Fig. 14 we show the normalized densities and interface acceleration as functions of time. The shock at t = 0 compresses the He and air densities by ~ 1.5. They stay constant until 4.8 ms when the rarefaction meets the interface. The acceleration, being essentially a delta-

function in time ($g = \Delta v \delta(t)$), is zero until that time when it jumps to ~ 20 cm/ms^2 and then decays as the He and air decompress.

Snapshots of the interface region at 4.2, 4.6, 5.0, and 5.4 ms are shown in Fig. 15. We bypass earlier snapshots as they are identical to the shock/reshock case and can be seen in Fig. 5 of Ref. 20. The bubble amplitude as a function of time is presented in Fig. 16 comparing CALE (dashed line) and GLM (continuous). As discussed in Ref. 20, the postshock evolution is well represented by Eq. (3) with $\eta_0 = \eta_{0+} = (1 - \Delta v / W_i)\eta_{0-}$, where $\Delta v \approx 15.8$ cm/ms, $W_i \approx 121$ cm/ms, and η_{0-} = 0.7 cm. For $\dot{\eta}_0$ we use Richtmyer's prescription,[4]

$$\dot{\eta}_0 = \eta_{0+} k \Delta v A_{after} \tag{12}$$

with $A_{after} \approx 0.77$. k_L is given by Eq. (7). The GLM calculation shown in Fig. 16 started after the passage of the initial shock and we used the above values of η_{0+} and $\dot{\eta}_0$ as initial conditions to Eqs. (8) and (9). As before,[20] the Layzer model slightly overestimates the effect of the shock and, from Fig. 16, we see that it tends to underestimate the effect of the rarefaction. The deviations from CALE are about 10–15%.

Note that the evolution of $\eta(t)$ after the rarefaction is effectively linear with time, meaning a constant bubble velocity v_b. It is well-known that in the classical RT instability with constant acceleration and densities $v_b \sim const.$ In the case of a rarefaction, however, neither the acceleration nor the densities are constant – see Fig. 14. Decreasing accelerations and decreasing densities (decompression) have opposite influences on $\eta(t)$, the net effect being a cancellation of opposing trends, leaving us with a constant v_b.

B. Air/He

This is the same system as considered in Sec. II (see Figs. 2 and 3) with the solid endwall replaced by a membrane. Therefore, instead of a reflected shock hitting the interface at $t \approx 2$ ms, it is now a rarefaction that accelerates the system downwards. Since the acceleration is directed from the heavier fluid (air) towards the lighter one (He), we expect and indeed find a phase reversal shortly after 2 ms. The acceleration and densities are shown in Fig. 17.

Snapshots of the interface, as calculated by CALE with $\eta_0 = 0.35$ cm are shown in Fig. 18. Note that there are two phase reversals, the first associated with the incident shock (always moving down in this paper) and the second with the rarefaction (moving up). Needless to say, with shock/rarefaction there is either no reversal (e.g., He/air) or two reversals (e.g., air/He), while with shock/reshock there is always one and only one phase reversal.

The "bubble" amplitude as calculated by CALE is shown in Fig. 19. We put bubble in quotation marks because it becomes a "spike" after a phase reversal. The amplitude shown in Fig. 19 (as in previous such figures) is obtained by a tracer particle at $x = 6.5$ cm on the interface. In the same figure we display the GLM result starting at $t = 0.2$ ms with $\eta_0 = 0$ and $\dot{\eta}_0$ given by Eq. (5a). As expected, it shows good agreement with CALE for the shock-induced bubble growth (where we could have used Eq. (3) as well) and the very early part of phase reversal. However, our solution fails to converge after $t \sim 2.4$ ms. This and other failures of the GLM are discussed in the Appendix.

C. Gas-Curtain

The replacement, by now familiar, of the endwall by a membrane takes us from the shock/reshock numerical experiment[17] to shock/rarefaction. (The effect of an isolated rarefaction was studied in the previous section—see Fig. 13). Needless to say, the evolution of the curtain

until the second wave hits it is the same as before. Therefore, we display in Fig. 20 only the evolution after the rarefaction, which occurs at about 600 μs. Comparing Fig. 20 with the case of a reshock (Fig. 16 in Ref. 17), we see that the rarefaction is much less disruptive to the curtain than a reshock. We remind the reader that neither reshock nor rarefaction experiments on gas-curtains have been performed to date.

We conclude this section by noting that in all our examples we have relied on what may be called "natural timing" for the rarefaction: By allowing the interface to be shocked first, and allowing the transmitted shock to burst the membrane that initiates the rarefaction, the upward moving rarefaction meets the downward moving interface at a set time, determined largely (but not solely) by the initial membrane-to-interface distance: 122 cm or 15 cm in our examples. It is possible, however, to burst the membrane by mechanical means anytime before the arrival of the transmitted shock; thus we shorten the time between the shock and the rarefaction or zero it out completely, i.e., the rarefaction and the shock can arrive simultaneously at the interface. If we further "delay" the shock, then the interface sees the rarefaction *before* the shock, a possibility studied in the next Section.

V. Rarefaction/Shock

Of the infinitely many configurations that can be obtained with an arbitrary time delay between the rarefaction and the shock, we will study only the air/He case for reasons that will soon become clear.

A. Air/He

Figures 9 and 10 displayed the air/He interface and the "bubble" amplitude as a function of time after the rarefaction reached the interface - it essentially oscillates with time. Having an arbitrary time delay at our disposal, we must decide at what time to send the shock. We shall

take advantage of this freedom to check a prediction of Eq. (1) which, as far as we know, has never been tested before.

Considering Fig. 10, at least two time-delays suggest themselves. The first is at ~0.56 ms, when the oscillating η (with η_0=0.7 cm) goes through zero. The second is at ~1.3 ms, when $|\eta|$ has a maximum. An interesting deduction from Eq. (1) is that if η_s=0 then the shock has no effect, as we discussed in the Introduction. Thus we expect little or no change in $\eta(t)$ for the "early" (0.56 ms) shock, and a relatively large change for the "late" (1.3 ms) shock, all compared with the no-shock case (Fig. 10).

For completeness, we show in Figs. 21a and 21b the interface acceleration and the gas densities for the early and late shocks separately, to be compared with Fig. 8 for the no-shock case. Although the densities and average accelerations are similar to the no-shock case, we should point out that the early and late shocks induce a $\Delta v \approx 14$ and 13 cm/ms respectively, and it is of course this Δv that appears in Eq. (1). The post-shock oscillations seen in the interface accelerations in Figs. 21a and 21b are due to sound waves as the transmitted shock moves down the previously rarefied He and, moving down a density gradient, sends sound waves back to the interface. Different zoning schemes and different choices for the artificial-Q in the code affected only the details of these sound waves, which we believe are physical.

The evolution of the amplitude in the no-shock case was shown in Fig. 10 and is repeated in Fig. 22 (curve 1) to which we add the early- and late-shock results (curves 2 and 3). Our expectations are indeed confirmed by this figure: The early shock, seeing $\eta_s \approx 0$, has practically no effect on η, while the late shock at $t \approx 1.3$ ms sees a large $|\eta_s|$ and almost immediately induces a phase reversal and growth to about twice the no-shock case (η ~ 6 cm vs. ~3 cm). In

all cases, the amplitudes succumb to the subsequent stable acceleration forcing them to oscillate, reminiscent of gravity waves.

Returning to the pure rarefaction case, Fig. 10, one sees a second "null" point at $t \approx 2.02$ ms when η goes through zero a second time. And indeed, when we further delayed the shock (always $M_s = 1.2$ in air) to reach the interface at this time, the subsequent evolution was very close to the no-shock case, confirming again that shocks seeing $\eta_s = 0$ have no effect on η or $\dot{\eta}$.

We will not consider rarefaction/shock in the other two systems, He/air and gas-curtain, because perturbations evolve uniformly in these cases (see Figs. 6 and 13 respectively) and no particular shock timing is preferred. Clearly, a shock arriving *after* the rarefaction has had time to amplify the perturbations will induce great vorticity and perhaps even turbulent mix. For example, Fig. 13 showed the gas-curtain undergoing a rarefaction. When we hit that curtain with a Mach 1.2 shock at $t = 300$ μs, the subsequent evolution is much accelerated so that at $t = 475$ μs (meaning 475 μs after rarefaction arrival but 175 μs after shock arrival) the curtain looks very much like the 600 μs curtain shown in Fig. 13, with densities about 50% higher than the pure rarefaction case shown in that figure.

VI. Conclusions

In this paper we have considered two opposite extremes at the end of a shock tube: a solid wall or a membrane. They may be called a "fixed" and a "free" boundary, respectively, and are "inverses" of each other in the sense discussed earlier[31] ("fixed-free theorem"). The solid endwall is standard practice, we believe, in all shock tubes. Its inverse, a "free" boundary, is a new consideration that can probably be easily implemented, leading to a much richer variety

of shocks and rarefactions occurring in different orders and timings. We have described a few possibilities in the preceding Sections.

There is clearly a continuum between these two extremes: a fluid, call it "C", so that depending on the properties of C the shock transmitted from A into B is reflected either as a shock or a rarefaction. For example, C can act as a "shock absorber" and thus reflect a weaker shock than a fixed boundary would. It can be shown that such weaker reshocks are necessary for certain kinds of freeze-out. Needless to say, the possibilities for C are endless and one must design experiments tailored to observe specific phenomena.

On the theory side, a surprise finding (see Ref. 25 and the Appendix) is the failure of the Layzer model for both stable and unstable accelerations for moderate or large values of $\eta_0 k$. For stable accelerations, we know of no example where the model does better than its linear limit, Eq. (11). The model fails at moderate values of $\eta_0 k$ like 1/3. For unstable accelerations where the model has traditionally been applied it appears to be valid for larger values of $\eta_0 k$, but up to a certain limit given by Eq. (A24). Beyond that limit the model fails again.

As discussed in the Introduction, complex acceleration histories are the hallmark of ICF implosions. We have illustrated several possible experiments in shock tubes with fixed or free boundaries where the interface between two fluids A/B is subjected to shocks and accelerations and decelerations. We believe experiments validating (or, perhaps more importantly, falsifying) code predictions concerning the evolution of interface perturbations will be invaluable when we apply the same codes to predict the presence or absence of mix in ICF nested shells, an issue of great impact on thermonuclear burn.[2] Just as in this paper code calculations have highlighted the shortcomings of the Layzer model, it is quite possible that experiments will reveal the shortcomings of code calculations.

Acknowledgement

This work was performed under the auspices of the U.S. Department of Energy by Lawrence Livermore National Laboratory under Contract DE-AC52-07NA27344.

APPENDIX: GENERALIZED LAYZER MODEL

A. Derivation

We consider two semi-infinite fluids of densities $\rho_A(t)$ and $\rho_B(t)$ in a gravitational field $g(t)$ in the y-direction. The interface is given by $y = y_{\text{int}}(x)$. We assume potential flow, $\phi_{A,B}(x,y,t)$, within each fluid. Within their respective regions the potentials satisfy Poisson's equation,

$$\nabla^2\phi + \frac{\dot{\rho}}{\rho} = 0\,, \tag{A1}$$

where we have omitted the subscript labels A or B. At the interface they satisfy

$$\partial_t y + \frac{\partial\phi}{\partial x}\frac{\partial y}{\partial x} - \frac{\partial\phi}{\partial y} = 0 \tag{A2}$$

for $y = y_{\text{int}}(x)$ and $\phi = \phi_A$ or ϕ_B. Finally, the potentials satisfy Bernoulli's equation,

$$\rho_A\left[\frac{\partial\phi_A}{\partial t} + \frac{1}{2}\left(\frac{\partial\phi_A}{\partial x}\right)^2 + \frac{1}{2}\left(\frac{\partial\phi_A}{\partial y}\right)^2 + gy\right] - (A \to B) = f(t) \tag{A3}$$

again at $y = y_{\text{int}}(x)$. Here $f(t)$ is an arbitrary function of time, and we have assumed that there are no spatial density gradients ($\vec{\nabla}\rho = 0$) except of course at the interface. This approach can be traced back to Bell[28] and is often adopted to accommodate time-dependent densities, taking $\rho_A(t)$, $\rho_B(t)$, and $g(t)$ as "givens" of the problem. The "unknowns" are ϕ_A, ϕ_B, and $y_{\text{int}}(x)$.

There are other models[29,30], besides Layzer's, which may be generalized to time-dependent densities and accelerations. We selected Layzer's model because of its simplicity and wide use. In Layzer's approach the above equations are satisfied not for all x but only in the vicinity of the bubble, $x \approx 0$:

$$y_{\text{int}} = \eta(t) + \eta_2(t)x^2 \tag{A4}$$

where $\eta(t)$ is the bubble amplitude (initial value = $\eta(0) \equiv \eta_0$) and $\eta_2(t)$ is related to the bubble curvature. Higher-order terms are neglected. Following Ref. 11, 2D and 3D flows are distinguished by a single parameter c ($\tilde{c}_g$ in Ref. 11). For 2D or "curtain" configuration the initial interface is given by

$$y_{\text{int}}(t=0) = \eta_0 \cos(kx_0) = \eta_0 (1 - c\frac{k^2 x_0^{\,2}}{4} + \ldots) \tag{A5a}$$

and for 3D or "tubular" flow

$$y_{\text{int}}(t=0) = \eta_0 J_0\left(\beta_n r_0 / R\right) = \eta_0 (1 - c\frac{k^2 x_0^{\,2}}{4} + \ldots) \tag{A5b}$$

where J_0 is the Bessel function of order zero, β_n are the zeros of the Bessel function of order one ($\beta_1 \approx 3.832, \beta_2 \approx 7.016, \beta_3 \approx 10.173, \ldots$), and R is the tube radius. We have let $x = r$ and $k = \beta_n / R$ for 3D. By expanding the cosine and Bessel functions we see that c = 2 for 2D and c = 1 for 3D. With the proper identification of the wavenumber k ($2\pi/\lambda$ for 2D, β_n / R for 3D) the value of c (2 for 2D, 1 for 3D) differentiates 2D from 3D flow.

The last step is to write down the potential in each fluid, valid to second order in x. This was done in Ref. 11 for a single (we'll call it B) fluid, and the extension to two fluids is straightforward:

$$\phi^B = \frac{a(t)}{k}(1 - c\frac{k^2 x^2}{4}) e^{-k(y-\eta)} - \frac{\dot{\rho}_B}{2\rho_B} y^2, \tag{A6}$$

$$\phi^A = \frac{b_1(t)}{k}(1 - c\frac{k^2 x^2}{4}) e^{k(y-\eta)} + b_2(t) y - \frac{\dot{\rho}_A}{2\rho_A} y^2, \tag{A7}$$

with $a(t)$ and $b_{1,2}(t)$ functions of time yet to be determined. This is the simplest extension of the original Layzer model (one fluid with constant density) to two fluids with time-dependent

densities and we refer to it as the "Generalized Layzer Model." By construction the potentials satisfy Poisson's equation, Eq. (A1), and have enough functions to satisfy Eqs. (A2) and (A3), always to second-order in x and near $y \sim y_{\text{int}}(x)$. The final results are given in Eqs. (8) and (9) as two ordinary, albeit nonlinear, coupled differential equations for $\eta(t)$ and $\eta_2(t)$.

We briefly outline the derivation. Substituting Eq. (A6) in Eq. (A2) we find

$$a(t) = -\frac{1}{\rho_B}\frac{d}{dt}(\rho_B \eta) \tag{A8}$$

from the zero-order terms. From the second-order terms we obtain Eq. (8). Note that this equation is identical to Eq. (5) of Goncharov and Li[11] as we have not (yet) used Eq. (A7) for the second fluid (all our results reduce to theirs for a single fluid).

Substituting Eq. (A7) in Eq. (A2) we find

$$b_1(t) + b_2(t) = \frac{1}{\rho_A}\frac{d}{dt}(\rho_A \eta) \tag{A9}$$

from the zero-order terms, and Eq. (10) from the second-order terms.

A much longer calculation is needed to obtain the last remaining equation, Eq. (9), from Bernoulli's equation, Eq. (A3), after substituting Eqs. (A6) and (A7) in it. The zero-order terms give $f(t)$, which we do not write down, and the second-order terms give Eq. (9), completing the derivation of the two equations, Eqs. (8) and (9), needed to solve for $\eta(t)$ and $\eta_2(t)$. Eq. (8) being a first-order ODE and Eq. (9) a second-order ODE we reduce them to a system of three first-order equations in a standard way (define $\dot{\eta}$ to be a new variable) and solve them numerically. Although three initial conditions, η_0, $\dot{\eta}_0$, $\eta_2(0)$ are needed, the last one is given by Eq. (A5)

$$\eta_2(0) = -ck^2\eta_0/4, \tag{A10}$$

so that only η_0 and $\dot{\eta}_0$ are needed as initial conditions. We usually set $\dot{\eta}_0$=0 (perturbations starting from rest), leaving only η_0.

We complete the derivation by comparing with previous results. As mentioned above, Eqs. (8) and (9) reduce to the results of Ref. 11 for a single fluid ($\rho_A = 0$). For two fluids of constant densities (see below) they reduce to the results of Ref. 10. For a single, constant density fluid with arbitrary η_0 we recover the 2D and 3D results of Ref. 8, confirmed by Ref. 9 for 2D. Finally, we recover Layzer's 2D and 3D results by setting $\eta_0 = 0$.

B. Linear Limit

We have not found any exact analytical solutions to the GLM equations. Only by going to the constant-density limit do we find analytic solutions reported previously.[8,20] To find analytic solutions for *time-dependent densities* we must resort to another limit, the linear limit, given by Eq. (11). We believe these solutions have not been previously reported and, although limited to the linear regime, $\eta k << 1$, we found them highly useful as test problems to verify the numerical solutions to the fully nonlinear GLM equations.

Example 1. Densities that decrease or increase with time affect the evolution of the amplitude as displayed in Eq. (11): $\eta(t)$ responds to both accelerating forces and to expansions/compressions. In general, accelerations increase $\eta(t)$ while compressions decrease it. It should therefore be possible to play these two forces against each other so that they cancel completely leading to a new kind of freeze-out, meaning $\dot{\eta}(t) = 0$. From Eq. (11), a constant $\eta(t)$ is obtained if and only if

$$g(t)k = \frac{1}{\rho_B(t) - \rho_A(t)} \{\rho_B \frac{d^2}{dt^2}(\ln \rho_B) + \rho_A \frac{d^2}{dt^2}(\ln \rho_A)\} \qquad \text{(A11)}$$

which we refer to as the freeze-out condition. One may use it to define $g_{freeze-out}$ if the densities are "given". If $g(t)$ is "given" then Eq. (A11) is a condition on $\rho_{A,B}$ to achieve freeze-out. For example, take a single fluid ($A=1$) and a constant g. The classical, meaning constant-density result is $\eta(t)=\eta_0\cosh(\sqrt{gk}t)$. On the other hand, if we allow the density to vary with time as $\rho(t)=\rho_0 e^{gkt^2/2}$, then $\eta(t)=\eta_0$ is the solution to Eq. (11): Acceleration and compression have cancelled each other out completely. In Fig. 23 we display the evolution of η/η_0, often called the growth factor, as a function of $\sqrt{gk}t$, often called the e-folding time. The nonlinear results, based on Eqs. (8) and (9), are also included. Of course freeze-out requires extreme compression: By 5 e-folding time the density must increase by $e^{12.5}\sim 2.7\times 10^5$. Large compressions are found only in ICF implosions[2] where the central DT, initially in vapor form, compresses by factors 10^5-10^6.

Unfortunately, this freeze-out condition (Eq. (A11)) depends on k and is therefore less interesting than the k-independent freeze-out reported in Ref. 15.

Example 2. Assuming that $g=const$ and that the densities vary exponentially with time, i.e.,

$$\rho_{A,B}(t)=\rho_{A,B}(0)e^{\alpha t}, \tag{A12}$$

Eq. (11) reduces to

$$\ddot{\eta}+\alpha\dot{\eta}-gkA\eta=0 \tag{A13}$$

with $A=$Atwood number $=\dfrac{\rho_B-\rho_A}{\rho_B+\rho_A}=\dfrac{\rho_B(0)-\rho_A(0)}{\rho_B(0)+\rho_A(0)}$. The solution is

$$\eta(t)=\eta_0\frac{\gamma_+e^{\gamma_-t}-\gamma_-e^{\gamma_+t}}{\gamma_+-\gamma_-}+\dot{\eta}_0\frac{e^{\gamma_+t}-e^{\gamma_-t}}{\gamma_+-\gamma_-} \tag{A14}$$

where

$$\gamma_{\pm} = -\frac{\alpha}{2} \pm \sqrt{gkA + \alpha^2/4}\,. \tag{A15}$$

Clearly, we get the classical result $\pm\sqrt{gkA}$ for constant densities, i.e., α=0. For $gkA+\alpha^2/4<0$ we can define $\gamma_{\pm} = -\frac{\alpha}{2} \pm i\omega$ and Eq. (A14) can be written as

$$\eta(t) = e^{-\alpha t/2}\{\eta_0 \cos(\omega t) + (\alpha\eta_0/2 + \dot{\eta}_0)\frac{\sin(\omega t)}{\omega}\} \tag{A16}$$

where $\omega = \sqrt{\left|gkA + \alpha^2/4\right|}$. We have damped oscillations for compressions ($\alpha > 0$), but growing oscillations for expansions ($\alpha < 0$), a type of behavior seen in the air/He rarefaction experiment (Figs. 8 through 12). For $gkA+\alpha^2/4>0$ we replace the sine and cosine functions in Eq. (A16) by their corresponding hyperbolic functions, leading to exponential growth in all cases except when gkA < 0 and $\alpha > 0$ (compression) where η decays exponentially with time.

<u>Example 3</u>. Consider the case $g = 0$. All that is required to solve Eq. (11) analytically is that $\rho_A(t)$ and $\rho_B(t)$ have the *same* functional form, hence $\rho_B(t)/\rho_A(t) = \rho_B(0)/\rho_A(0)$, which includes the single-fluid case (vanishing ρ_A or ρ_B). Under this assumption Eq. (11) can be written as $\frac{1}{\rho}\frac{d}{dt}(\rho\eta)$ = constant and its solution is

$$\eta(t) = \frac{1}{\rho(t)}\{\rho_0\eta_0 + \frac{1}{\rho_0}\left(\frac{d}{dt}(\rho\eta)\right)_0 \int_0^t \rho dt\} \tag{A17}$$

where $\rho(t) = \rho_A(t)$ or $\rho_B(t)$, and $\rho_0 = \rho_A(0)$ or $\rho_B(0)$. If $\rho(t) \sim e^{\alpha t}$ then $\eta(t) = \eta_0 + \frac{\dot{\eta}_0}{\alpha}(1 - e^{-\alpha t})$.

C. Constant densities.

The rest of this Appendix is limited to time-independent density profiles. The first GLM equation, Eq. (8), can be solved analytically:

$$\eta_2(t) = \frac{ck}{4(1+c)}\left\{-1+[1-(1+c)\eta_0 k]e^{-k(1+c)(\eta-\eta_0)}\right\} \tag{A18}$$

where we have already used Eq. (A10) for $\eta_2(0)$. The second equation, Eq. (9) reduces to

$$\begin{aligned}&\left(\frac{ck^2}{2} - 2ckA\eta_2 - 8(1+1/c)A\eta_2{}^2\right)\frac{\ddot{\eta}}{k-4(1+1/c)\eta_2}\\ &+k^2\left(ck^2(3\frac{cA}{2}+A-c-1)/2 - 2(1+c)(1+2c-A-cA)k\eta_2 + 4(1+c)^2A\eta_2{}^2\right)\times\\ &\left(\frac{\dot{\eta}}{k-4(1+1/c)\eta_2}\right)^2 + 2gA\eta_2 = 0.\end{aligned} \tag{A19}$$

We now elaborate on our comparison with previous work: The above equation reduces to Goncharov's[10] Eqs. (8) and (18) for c=2 (2D) and c=1 (3D) respectively. For A=1 it reduces to Eqs. (2a) and (2b), respectively, of Ref. 8 after defining $\theta \equiv e^{(\eta-\eta_0)k}$ and, if $g = const.$, can be integrated once (see Eqs. (3a,b) in Ref. 8). If we further let $\eta_0 = 0$ we recover Layzer's results (his Eqs. (32) and (55)) by setting c=1 and c=2 respectively.

In the course of this investigation we discovered limitations and failures which occur even for constant densities (Eq. (A19)), and have reported them in a brief communication.[25] the first occurs for large η_0: Eq. (A19) gives an unphysical solution if the coefficient of its $\ddot{\eta}$ term vanishes. Write

$$\frac{ck^2}{2} - 2ckA\eta_2 - 8(1+1/c)A\eta_2{}^2 = -8(1+1/c)A(\eta_2-\eta_2{}^+)(\eta_2-\eta_2{}^-) \tag{A20}$$

where

$$\eta_2^{\pm} \equiv \frac{c^2 k}{8(1+c)}\left(-1 \pm \sqrt{1+\frac{4(1+c)}{Ac^2}}\right). \tag{A21}$$

Note that η_2 is always negative, varying between $\eta_2(0) = -ck^2\eta_0/4$ and $\eta_2(\infty) = -ck/4(1+c)$, while $\eta_2^{+} > 0$ and $\eta_2^{-} < 0$. Therefore $\eta_2 - \eta_2^{+}$ is also negative and cannot vanish. However, $\eta_2 - \eta_2^{-}$ can vanish, unless η_2^{-} is outside the range of $\eta_2(t)$, which requires

$$\eta_2^{-} < \eta_2(0), \tag{A22}$$

i.e.,

$$\frac{c^2 k}{8(1+c)}\left[-1-\sqrt{1+\frac{4(1+c)}{Ac^2}}\right] < -ck^2\eta_0/4 \tag{A23}$$

which can be written as

$$\eta_0 k < (\eta_0 k)_{\max} \equiv \frac{c}{2(1+c)}\left[1+\sqrt{1+\frac{4(1+c)}{Ac^2}}\right] \tag{A24}$$

as reported in Ref. 25. For $A=1$ this upper limit is $(\eta_0 k)_{\max} = 1$ independent of c. Indeed, by examining the only known analytic solutions for arbitrary $\eta_0 k$ (the case $A=1$ and $g=0$, Eqs. (10) through 15 of Ref. 8) we see that $\eta_0 k < 1$ is a necessary requirement for $A=1$. Larger values are allowed for $A<1$: See Fig. 1 of Ref. 25. For example, for $A=1/8$ and $c=2$, $(\eta_0 k)_{\max} = 2$.

Eqs. (A18) and (A19) undergo a tremendous simplification for $\eta_0 k = \eta^* k \equiv 1/(1+c)$: Eq. (A18) gives $\eta_2(t) = const. = \eta_2(0) = -ck/4(1+c)$ and Eq. (A19) can be written succinctly as a *linear* equation:

$$\ddot{\theta}_L - gk_L A_L \theta_L = 0 \tag{A25}$$

where

$$k_L \equiv c(1+c)(1+A)k/2(1+c+cA-A)\,, \tag{A26a}$$

$$A_L \equiv 2A/(1+c+cA-A)\,, \tag{A26b}$$

$$\theta_L \equiv e^{(\eta-\eta_0)k_L}\,. \tag{A26c}$$

Of course $\theta_L(0)=1$ and $\dot{\theta}_L(0)=\dot{\eta}_0 k_L$. Note the similarity of Eq. (A25) to Rayleigh's linear equation $\ddot{\eta}-gkA\eta=0$. For $g=const.$ the solution to Eq. (A25) is

$$\theta_L = \cosh(\gamma_L t)+\frac{\dot{\theta}_L(0)}{\gamma_L}\sinh(\gamma_L t) \tag{A27}$$

where

$$\gamma_L \equiv \sqrt{gk_L A_L}\,. \tag{A28}$$

Eq. (A27) is equivalent to

$$\eta(t)=\eta_0+\frac{1}{k_L}\ln\left[\cosh(\gamma_L t)+\frac{\dot{\eta}_0}{\dot{\eta}_\infty}\sinh(\gamma_L t)\right] \tag{A29}$$

where

$$\dot{\eta}_\infty \equiv \gamma_L/k_L=\sqrt{gA_L/k_L}=2\sqrt{\frac{gA}{c(1+c)(1+A)k}} \tag{A30}$$

is the asymptotic RT bubble velocity.

If $g=0$ as is the case after a shock and therefore labeled the RM case, we take the $g\to 0$ limit of Eq. (A29):

$$\eta(t)=\eta_0+\frac{1}{k_L}\ln(1+\dot{\eta}_0 k_L t)\,, \tag{A31}$$

which is Eq. (3). Now the bubble velocity is a decreasing function of time,

$$\dot{\eta}(t)=\frac{\dot{\eta}_0}{1+\dot{\eta}_0 k_L t}=\frac{\dot{\eta}_0}{1+\dot{\eta}_0/\dot{\eta}_\infty} \tag{A32}$$

with the asymptotic value

$$\dot{\eta}_\infty = 1/k_L t \tag{A33}$$

as in Eq. (4).

One can find other analytic solutions to Eq. (A25) by using other time-dependent accelerations $g(t)$ as was done in Ref. 25, always with the *proviso* that the solutions θ_L be positive definite. We know of no other nonlinear model that can provide explicit solutions for the nonlinear amplitude for nontrivial $g(t)$.

An additional advantage of Eq. (A25) is the following: As we have already pointed out, Eqs. (A25) through (A33) give satisfactory results for other values of η_0 also.[8] So far the emphasis has been on the *simplicity* of Eq. (A25) *vis-à-vis* Eq. (A19) and the explicit solutions for RT and RM instabilities, Eqs. (A29) and (A31) respectively. Eq. (A25), however, becomes incomparably better than Eq. (A19) when the latter fails, and it can do so rather dramatically. As discussed above and in Ref. 25, Eq. (A19) fails for $\eta_0 \geq (\eta_0)_{\max}$. Using Eq. (A25), on the other hand, one obtains results which, although not quite correct, are not patently wrong as Eq. (A19) can be. For example, in Ref. 25 we discussed a *gedanken* LEM experiment in which a single fluid ($A = 1$) with surface perturbations of $\lambda = 7.3/3$ cm is accelerated, hence $(\eta_0)_{\max} = 1/k = 7.3/6\pi \approx 0.4$ cm. The acceleration increases from 0 to $70g_0$ ($g_0 = 0.98\times10^{-3}$ cm/ms^2) in 7 ms, after which it is kept constant at that value. Three different initial amplitudes were considered: 0.13, 0.3, and 0.5 cm. For the first η_0 Eqs. (A19) and (A25) give identical $\eta(t)$ because $\eta_0 k = 1/3$, i.e., $\eta_0 = \eta^*$, and the result agrees well with CALE simulations (See Fig. 4 in Ref. 25). For the second η_0 Eqs. (A19) and (A25) give comparable results that agree, within 10-15%, with CALE. For the third η_0 (0.5 cm) however, Eq. (A19)

fails miserably because now $\eta_0 > (\eta_0)_{\max}$. In Fig. 24 we display these results comparing CALE, Eq. (A19), and Eq. (A25). Eq. (A19) is patently wrong for this η_0, while Eq. (A25), admittedly not in perfect agreement with CALE, gives a perhaps acceptable result. At this time we have no better proposition than using Eq. (A25) for instabilities with $\eta_0 > (\eta_0)_{\max}$.

In Figs. 10 and 12 we pointed out that the GLM fails for negative gA, particularly for large $\eta_0 k$ (but of course always within the allowed region, i.e., $\eta_0 k < (\eta_0 k)_{\max}$). For very small ηk the GLM reduces to the linear theory, Eq. (11), valid for both positive and negative gA. For negative gA the GLM begins to fail as ηk increases. The reason can be found in Eq. (A25): For $gA < 0$ the solution to Eq. (A25) oscillates in time ($\theta_L \sim \sin \omega_L t$ or $\cos \omega_L t$) just like the linear gravity waves ($\eta \sim \sin \omega t$ or $\cos \omega t$ is the solution to $\ddot{\eta} - gkA\eta = 0$ for $gA < 0$). However, from its definition (Eq. (A26c), θ_L is a positive definite variable and cannot change sign. In other words for $gA < 0$ the cosh and sinh terms in Eq. (A29) go over to cos and sin and one is soon taking the logarithm of a negative number resulting in imaginary η!

The third type of failure reported in Ref. 25 deals with models for spikes as advocated in Refs. 9 and 10. In this paper we do not consider spikes because there is no satisfactory spike model for arbitrary A even for the standard, constant-density Layzer model.[25]

REFERENCES

[1]B. Fryxell, E. Müller, and D. Arnett, "Instabilities and clumping in SN 1987A. I. Early evolution in two dimensions," Ap. J. **367**, 619 (1991); D. Arnett, *Supernovae and Nucleosynthesis*, Princeton University Press, Princeton, 1996; B. A. Remington, R. P. Drake, and D. D. Ryutov, "Experimental astrophysics with high power lasers and Z pinches," Rev. Mod. Phys. **78**, 755 (2006).

[2]J. D. Lindl, *Inertial Confinement Fusion* (Springer, New York, 1998); P. W. Mckenty, V. N. Goncharov, R. P. J. Town, S. Skupsky, R. Betti, and R. L. McCrory, "Analysis of a direct-drive ignition capsule designed for the National Ignition Facility," Phys. Plasmas **8**, 2315 (2001); R. Betti, C. D. Zhou, K. S. Anderson, L. J. Perkins, W. Theobald, and A. A. Solodov, "Shock ignition of thermonuclear fuel with high areal density," Phys. Rev. Lett. **98**, 155001 (2007).

[3]Lord Rayleigh, *Scientific Papers*, **2**, (Dover, New York, 1965); G. I. Taylor, "The instability of liquid surfaces when accelerated in a direction perpendicular to their planes, I," Proc. R. Soc. London Ser. A **201**, 192 (1950).

[4]R. D. Richtmyer, "Taylor instability in shock acceleration of compressible fluids," Commun. Pure Appl. Math. **13**, 297 (1960); E. E. Meshkov, "Instability of the interface of two gases accelerated by a shock wave," Fluid Dyn. **4**, 101 (1969).

[5]D. H. Sharp, "An overview of Rayleigh-Taylor instability," Physica D **12**, 3 (1984); H. J. Kull, "Theory of the Rayleigh-Taylor instability," Phys. Rep. **206**, 197 (1991); M. Brouillette, "The Richtmyer-Meshkov instability," Ann. Rev. Fluid Mech. **34**, 445 (2002).

[6]W. S. Varnum, N. D. Delamater, S. C. Evans, P. L. Gobby, J. E. Moore, J. M. Wallace, R. G. Watt, J. D. Colvin, R. Turner, V. Glebov, J. Soures, and C. Stoeckl, "Progress toward ignition with noncryogenic double-shell capsules," Phys. Rev. Lett. **84**, 5153 (2000); P. Amendt, J. D. Colvin, R. E. Tipton, D. E. Hinkel, M. J. Edwards, O. L. Landen, J. D. Ramshaw, L. J. Suter, W. S. Varnum, and R. G. Watt, "Indirect-drive noncryogenic double-shell ignition targets for the National Ignition Facility: Design and analysis," Phys. Plasmas **9**, 2221 (2002).

[7]D. Layzer, "On the instability of superposed fluids in a gravitational field," Astrophys. J. **122**, 1 (1955).

[8]K. O. Mikaelian, "Analytic approach to nonlinear Rayleigh-Taylor and Richtmyer-Meshkov instabilities," Phys. Rev. Lett. **80**, 508 (1998).

[9]Q. Zhang, "Analytical solutions of Layzer-type approach to unstable interfacial fluid mixing," Phys. Rev. Lett. **81**, 3391 (1998).

[10]V. N. Goncharov, "Analytical model of nonlinear, single-mode, classical Rayleigh-Taylor instability at arbitrary Atwood numbers," Phys. Rev. Lett. **88**, 134502 (2002).

[11]V. N. Goncharov and D. Li, "Effects of temporal density variation and convergent geometry on nonlinear bubble evolution in classical Rayleigh-Taylor instability," Phys. Rev. E **71**, 046306 (2005).

[12]K. O. Mikaelian, "Richtmyer-Meshkov instabilities in stratified fluids," Phys. Rev. A **31**, 410 (1985).

[13]A. A. Charakhch'yan, "Reshocking at the non-linear stage of Richtmyer-Meshkov instability," Plasma Phys. Control. Fusion **43**, 1169 (2001).

[14]R. Courant and K. O. Friedrichs, *Supersonic Flow and Shock Waves* (Springer-Verlag, Berlin, 1948).

[15]K. O. Mikaelian, "Growth rate of the Richtmyer-Meshkov instability at shocked interfaces," Phys. Rev. Lett. **71**, 2903 (1993); "Freeze-out and the effect of compressibility in the Richtmyer-Meshkov instability," Phys. Fluids **6**, 356 (1994).

[16]R. E. Tipton, in *Megagauss Technology and Pulsed Power Applications*, edited by C. M. Fowler, R. S. Caird, and D. J. Erickson (Plenum, New York, 1987); R. T. Barton, in *Numerical Astrophysics*, edited by J. M. Centrella, J. M. LeBlanc, R. L. Bowers, and J. A. Wheeler (Jones and Bartlett, Boston, 1985).

[17]K. O. Mikaelian, "Numerical simulations of Richtmyer-Meshkov instabilities in finite-thickness fluid layers," Phys. Fluids **8**, 1269 (1996).

[18]J. W. Jacobs, D. L. Klein, D. G. Jenkins, and R. F. Benjamin, "Instability growth patterns of a shock-accelerated thin fluid layer," Phys. Rev. Lett. **70**, 583 (1993); J. M. Budzinski, R. F. Benjamin, and J. W. Jacobs, "Influence of initial conditions on the flow patterns of a shock-accelerated thin fluid layer," Phys. Fluids **6**, 3510 (1994); P. M. Rightley, P. Vorobieff, and R. F. Benjamin, "Evolution of a shock-accelerated thin fluid layer," Phys. Fluids **9**, 1770 (1997).

[19]Private communication by Kathy Prestridge.

[20]K. O. Mikaelian, "Explicit expressions for the evolution of single-mode Rayleigh-Taylor and Richtmyer-Meshkov instabilities at arbitrary Atwood numbers," Phys. Rev. E **67**, 026319 (2003).

[21]K. O. Mikaelian, "Richtmyer-Meshkov instability of arbitrary shapes," Phys. Fluids **17**, 034101 (2005).

[22]C. E. Niederhaus and J. W. Jacobs, "Experimental study of the Richtmyer-Meshkov instability of incompressible fluids," J. Fluid Mech. **485**, 243 (2003); J. W. Jacobs and V. V. Krivets, "Experiments on the late-time development of single-mode Richtmyer-Meshkov instability," Phys. Fluids **17**, 034105 (2005); P. R. Chapman and J. W. Jacobs, "Experiments on the three-dimensional incompressible Richtmyer-Meshkov instability," Phys. Fluids **18**, 074101 and 129902 (2006).

[23]K. A. Meyer and P. J. Blewett, "Numerical investigation of the stability of a shock-accelerated interface between two fluids," Phys. Fluids **15**, 753 (1972).

[24]M. Vandenboomgaerde, C. Mügler, and S. Gauthier, "Impulsive model for the Richtmyer-Meshkov instability," Phys. Rev. E **58**, 1874 (1998).

[25]K. O. Mikaelian, "Limitations and failures of the Layzer model for hydrodynamic instabilities," to appear in Phys. Rev. E.

[26]R. M. Baltrusaitis, M. L. Gittings, R. P. Weaver, R. F. Benjamin, and J. M. Budzinski, "Simulation of shock-generated instabilities," Phys. Fluids **8**, 2471 (1996); G. Weirs, V. Dwarkadas, T. Plema, C. Tomkins, and M. Marr-Lyon, "Validating the *Flash* code: Vortex-dominated flows," Astrophys. Space Sci. **298**, 341 (2005).

[27]K. O. Mikaelian, "Evolution of perturbations in shocked fluid layers," in *Proceedings of the Fifth International Workshop on Compressible Turbulent Mixing*, Stony Brook, N.Y., 1995, p. 363.

[28]G. I. Bell, "Taylor instability on cylinders and spheres in the small amplitude approximation," Los Alamos Scientific Laboratory Report No. LA-1321, 1951.

[29]J. A. Zufiria, "Bubble competition in Rayleigh-Taylor instability," Phys. Fluids **31**, 440 (1988).

[30]S. I. Abarzhi, K. Nishihara, and J. Glimm, "Rayleigh-Taylor and Richtmyer-Meshkov instabilities for fluids with a finite density ratio," Phys. Lett. A **317**, 470 (2003).

[31]K. O. Mikaelian, "Normal modes and symmetries of the Rayleigh-Taylor instability in stratified fluids," Phys. Rev. Lett. **48**, 1365 (1982); "Rayleigh-Taylor instabilities in stratified fluids," Phys. Rev. A **26**, 2140 (1982).

Figure Captions:

Fig. 1. A shock or rarefaction tube. With a solid endwall the perturbed A/B interface will undergo shock/reshock. With a membrane burst into vacuum the interface will see a rarefaction. The first shock may be launched before or after bursting the membrane, hence the interface will see a shock first followed by a rarefaction or *vice-versa*. We consider perturbed interfaces between He/air, air/He, and air/SF_6/air gas curtains.

Fig. 2. Snapshots of the air/He interface with perturbations of $\lambda = 13$ cm and $\eta_0 = 0.7$ cm. A Mach 1.2 shock moving down in air strikes the interface at $t = 0$, reflects off the endwall 122 cm away and, moving up, reshocks the interface at $t = 2.0$ ms, hence the last snapshot is 0.5 ms after reshock. The time-evolution of the bubble amplitude (at $x = 6.5$ or 19.5 cm) is shown in Fig. 3.

Fig. 3. Bubble amplitude as a function of time for the air/He problem shown in Fig. 2. The Mach 1.2 shock strikes the interface at $t = 0$ when the amplitude is $\eta_0 = $-0.35 cm or -0.7 cm (the negative sign is for plotting convenience). The dashed curves are from CALE simulations and include reshock at $t = 2$ ms. The continuous curves are from Eq. (3) — see text.

Fig. 4. The normalized densities and the interface acceleration as functions of time in ms for the He/air case undergoing a rarefaction. The densities are normalized by their initial values, $\rho_{He}(0) = 0.166$ mg/cm^3 and $\rho_{air}(0) = 1.2$ mg/cm^3. The interface acceleration, in cm/ms^2, is normalized by 10 for plotting convenience.

Fig. 5. Snapshots of the He/air interface under a rarefaction. The interface starts with perturbations of $\lambda = 13$ cm and $\eta_0 = 0.7$ cm. Snapshots at $t = 0$, 1.8, 2.6, and 3.8 ms. Compare with the shock case, Fig. 5 in Ref. 20.

Fig. 6. Bubble amplitude $\eta(t)$ as a function of time in ms for the He/air case undergoing a rarefaction, as calculated by CALE (dashed line) and GLM (continuous line), starting with $\eta_0 = 0.7$ cm. See Fig. 5 for snapshots of the interface. The GLM uses the acceleration and densities displayed in Fig. 4 as input to Eqs. (8) and (9).

Fig. 7. Same as Fig. 6 for $\eta_0 = 0.05$ cm. We have added the linear result, Eq. (11). For small amplitudes CALE (dashed line), GLM (continuous), and linear (continuous) results agree, but for $\eta > 1$ cm the linear result overestimates the growth.

Fig. 8. Same as Fig. 4 for the air/He case.

Fig. 9. Snapshots of the air/He interface under a rarefaction. The interface starts with perturbations of $\lambda = 13$ cm and $\eta_0 = 0.7$ cm. Snapshots at $t = 0$, 0.9, 1.3, 2, 2.9, and 3.3ms. Compare with the He/air case, Fig. 5

Fig. 10. $\eta(t)$ vs. t for the air/He case starting with $\eta_0 = 0.7$ cm. The dashed curve is the CALE result (snapshots in Fig. 9) and the continuous curve is the GLM result we believe to be completely erroneous. Compare with the He/air case, Fig. 6.

Fig. 11. Same as Fig. 10 with $\eta_0 = 0.05$ cm. The CALE result agrees with both the linear and nonlinear GLM. Compare with the He/air case, Fig. 7.

Fig. 12. Same as Fig. 10 with $\eta_0 = 0.35$ cm. The linear result is much closer to CALE than the nonlinear GLM.

Fig. 13. Snapshots of the air/SF_6/air gas-curtain system under a rarefaction. Twenty isodensity contours are displayed logarithmically spaced from 0.5 mg/cm^3 to 5 mg/cm^3. Compare with Fig. 10 of Ref. 17 for the shock case.

Fig. 14. The normalized densities and acceleration as functions of time in ms for the He/air case undergoing a shock at $t = 0$ followed by a rarefaction at 4.8 ms. The M_s = 1.2 shock increases the He and air densities ~1.5 times. They remain constant until the rarefaction reaches them.

Fig. 15. Isodensity contours for the He/air case undergoing shock/rarefaction, with the shock arriving at $t = 0$ and the rarefaction at $t = 4.8$ ms. The early evolution from $t = 0$ to 4.2 ms is identical to the shock/reshock case[20,21] and is not shown here. $\eta_0 = 0.7$ cm, $\lambda = 13$ cm.

Fig. 16. Bubble amplitude as a function of time for the He/air case undergoing shock/rarefaction. The dashed curve is the result of the CALE simulation (snapshots in Fig. 15), the continuous curve is from the GLM. The GLM overestimates the effect of the shock, but underestimates the rarefaction.

Fig. 17. Same as Fig. 14 for the air/He case. The M_s = 1.2 shock increases the densities ~1.2 times. They remain constant until the rarefaction reaches the interface at ~2 ms.

Fig. 18. Snapshots of the air/He interface undergoing a shock/rarefaction (see Fig. 17 for acceleration and densities). The initial amplitude is 0.35 cm. Compare with Fig. 2 for the shock/reshock case.

Fig. 19. "Bubble" amplitude for the air/He shock/rarefaction case. The interface with $\eta_0 = 0.35$ cm is shocked (M_s = 1.2) at $t = 0$. The transmitted shock exits into vacuum and sends back (i.e., up) a rarefaction wave that reaches the interface at $t \sim 2$ ms and reaccelerates the interface downward (see Fig. 17). Snapshots were given in Fig. 18. The dashed line is the CALE result, and the continuous line is the GLM result, which stops shortly after 2.4 ms.

Fig. 20. Snapshots of the air/SF_6/air gas-curtain undergoing a shock at $t = 0$ followed by a rarefaction. The curtain was initially 15 cm away from the endmembrane separating air from vacuum. The membrane bursts at $t \sim 350$ μs by the transmitted shock, and a rarefaction wave

moves up to meet the curtain at $t \sim 600$ μs. The effect of the shock before the rarefaction was measured experimentally (sinuous pattern, Ref. 18) and simulated with CALE (Ref. 17). Same isodensity contours as in Fig. 13.

Fig. 21. Air/He interface acceleration and gas densities as functions of time when a rarefaction is followed by (a): an early shock at 0.53 ms or (b): a late shock at 1.3 ms. Compare with the no-shock case, Fig. 8.

Fig. 22. $\eta(t)$ vs. t for three air/He rarefaction/shock cases discussed in the text: 1) no shock - this curve is the same as in Fig. 10; 2) Rarefaction at $t = 0$ followed by a shock at 0.56 ms (early); 3) Rarefaction at $t = 0$ followed by a shock at 1.3 ms (late). All CALE calculations. Arrows indicate shock arrival times for curves 2 and 3. In curve 2 the early (0.56 ms) shock sees $\eta_s = 0$ and therefore has no effect on the evolution of $\eta(t)$ (its later evolution differs from curve 1 because the acceleration histories are different).

Fig. 23. Linear and nonlinear growth factors η/η_0 as functions of e-folding time $\sqrt{gkt}$ in a single fluid ($\rho_A = 0$) taking $g = const.$ and $\eta_0 k = 0.1$. In the two upper curves the density is held constant; In the two lower curves $\rho = \rho(0)e^{gkt^2/2}$, leading to freeze-out in the linear theory given by Eq. (11). The nonlinear results are calculated from Eqs. (8) and (9).

Fig. 24. Bubble amplitude $\eta(t)$ in cm as a function of time in ms as calculated by CALE, Eq. (A19), and Eq. (A25). The system is a single-fluid LEM tank with perturbations of λ=7.3/3 cm and initial amplitude $\eta_0 = 0.5$ cm (see text for acceleration history). Eq. (A19) fails because $\eta_0 k > (\eta_0 k)_{\max}$ given by Eq (A24). For smaller values of η_0 both equations show fair agreement with CALE (see Ref. 25).

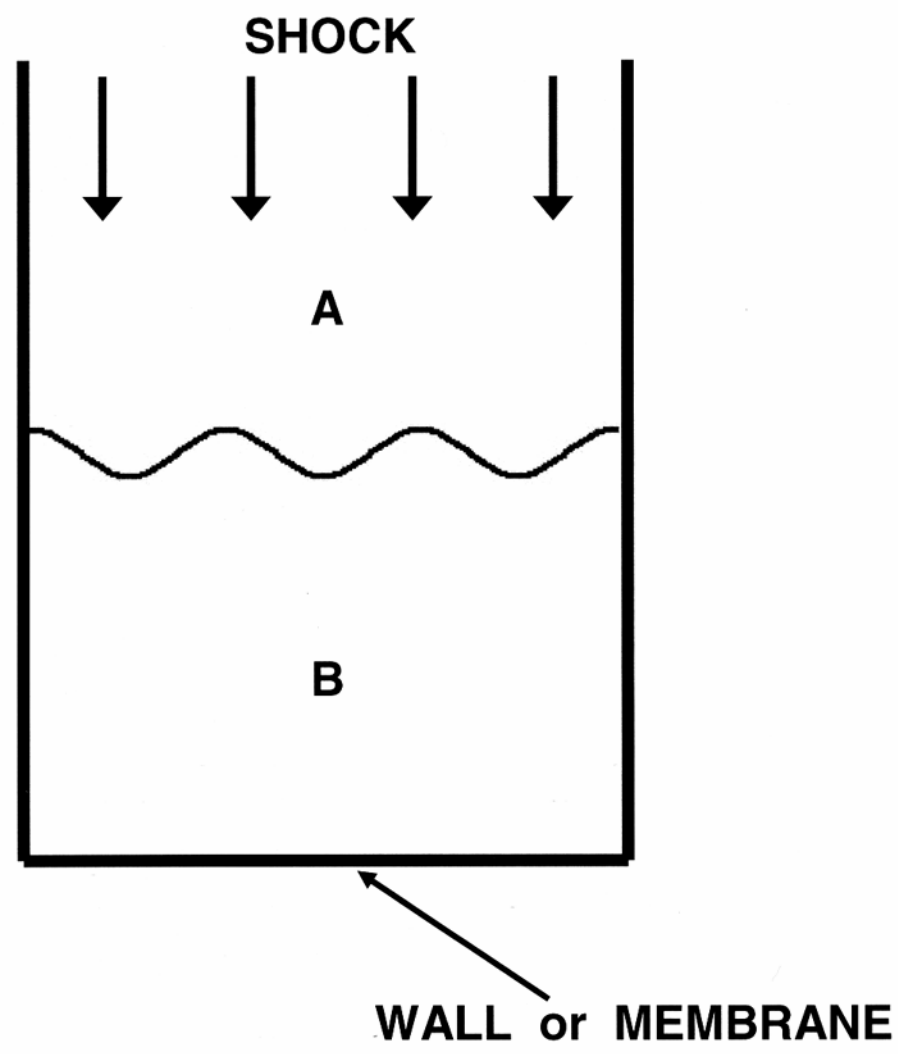

Fig. 1

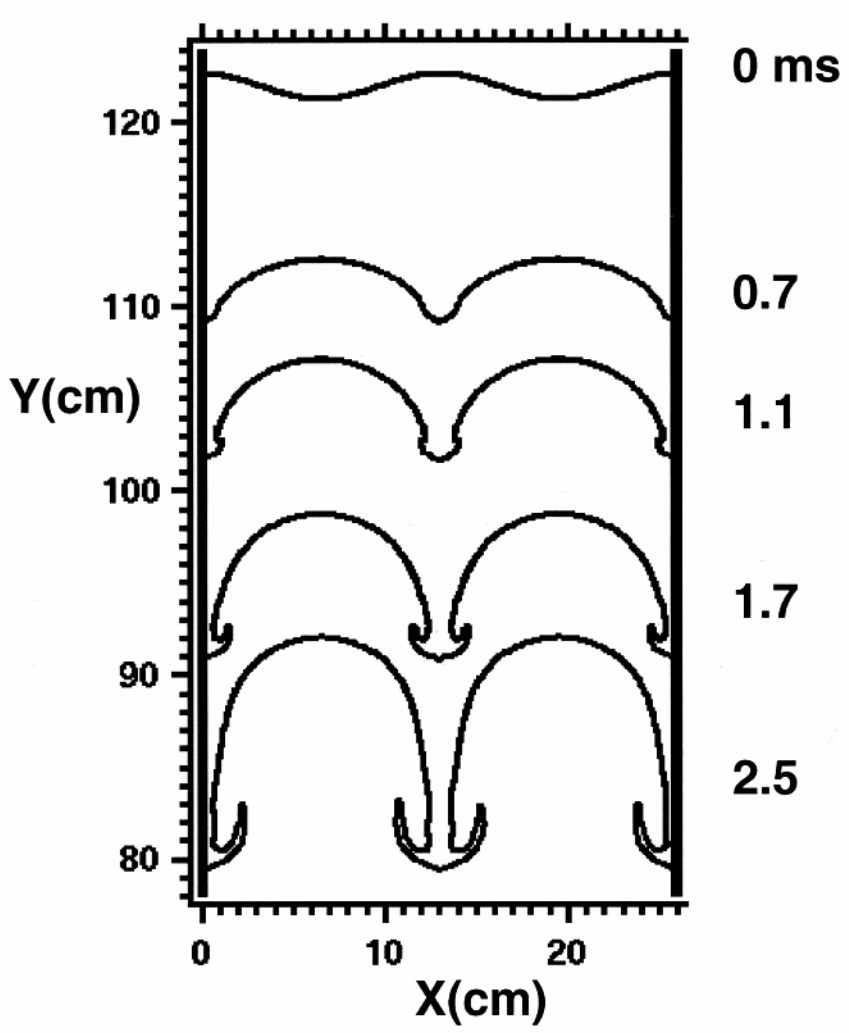

Fig. 2

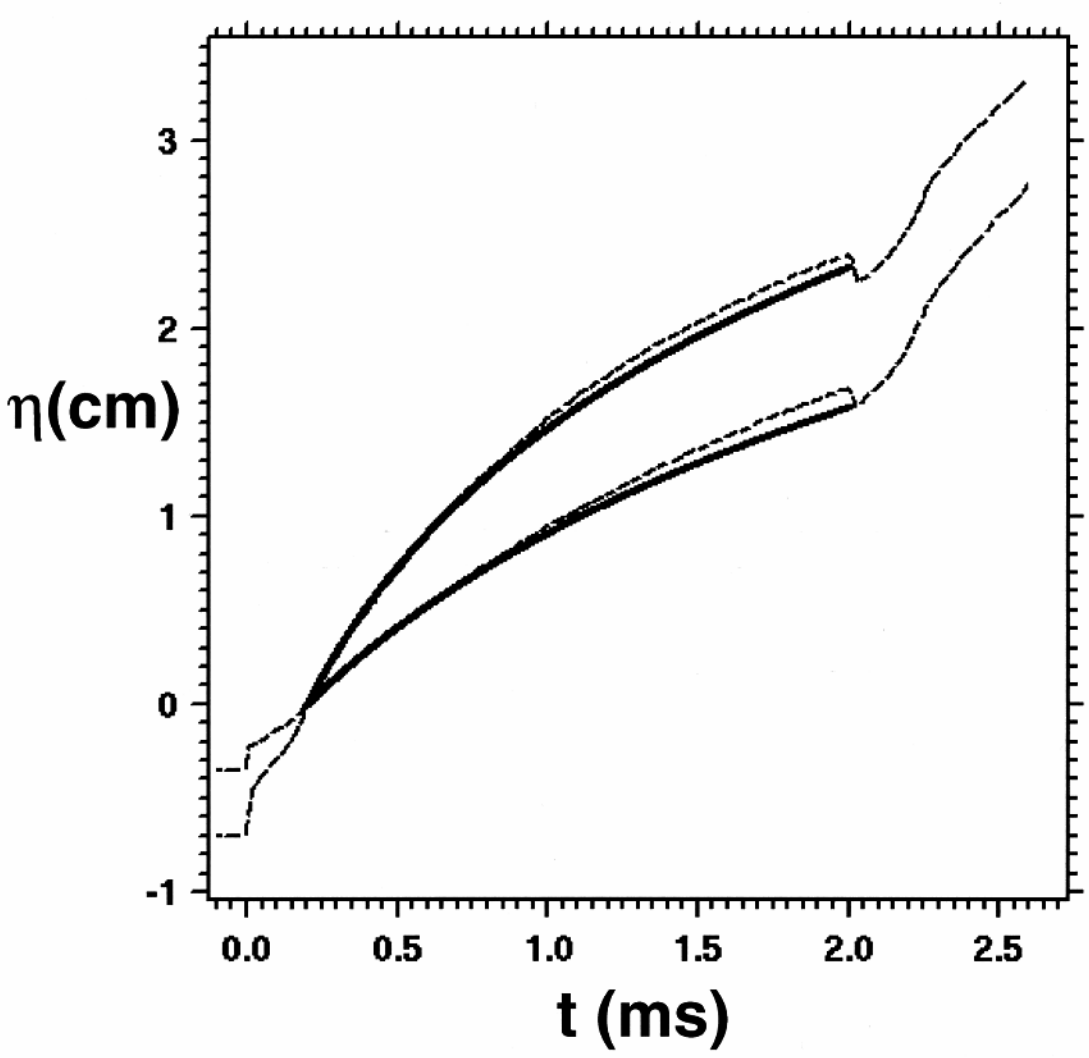

Fig. 3

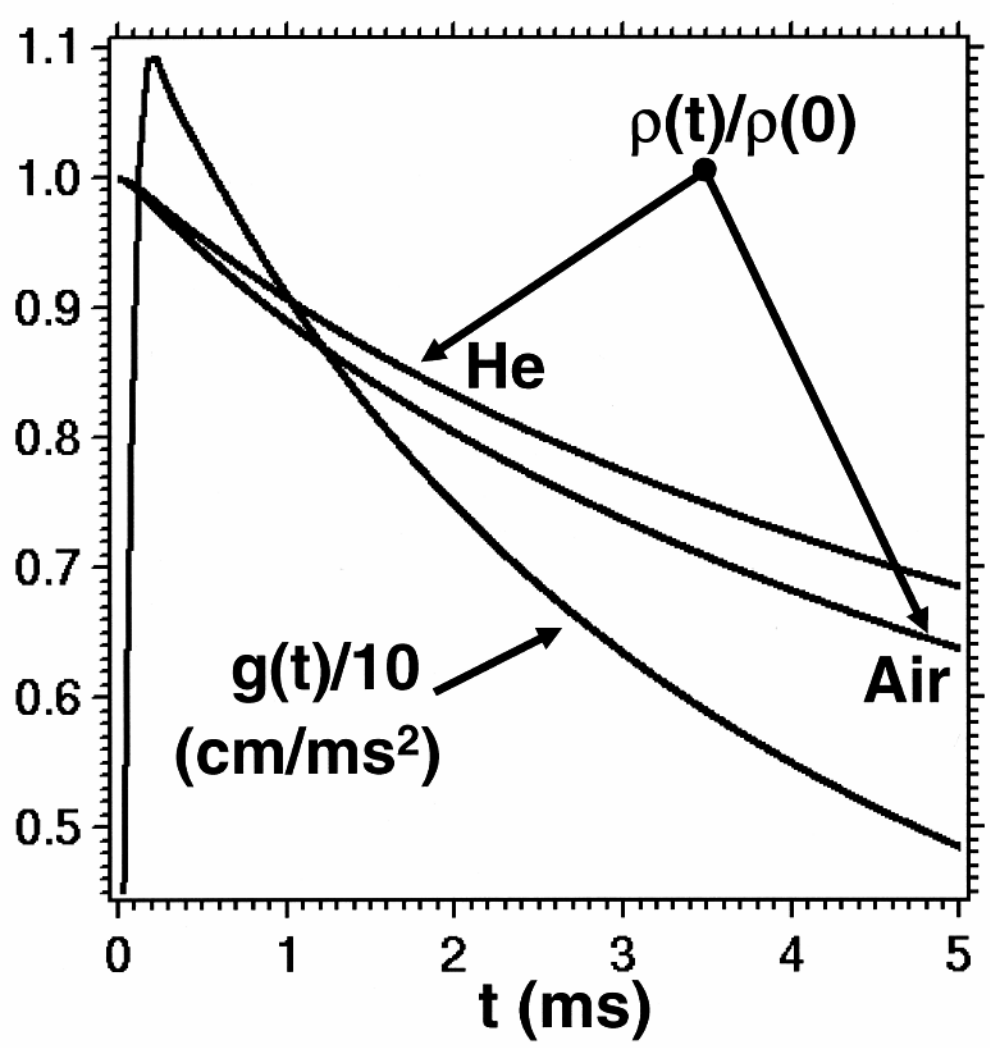

Fig. 4

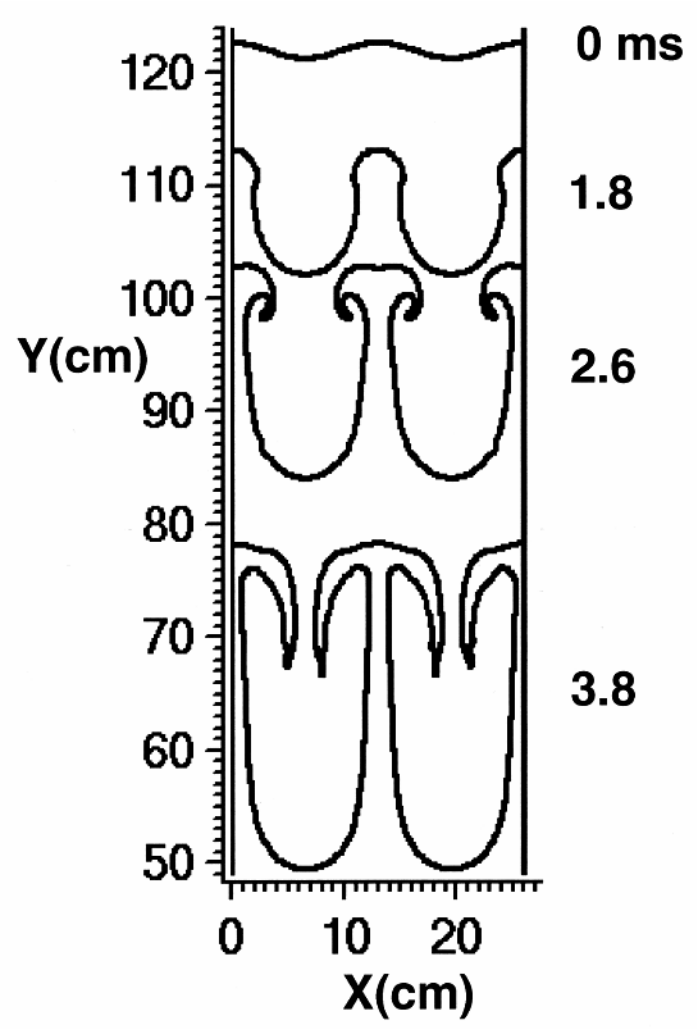

Fig. 5

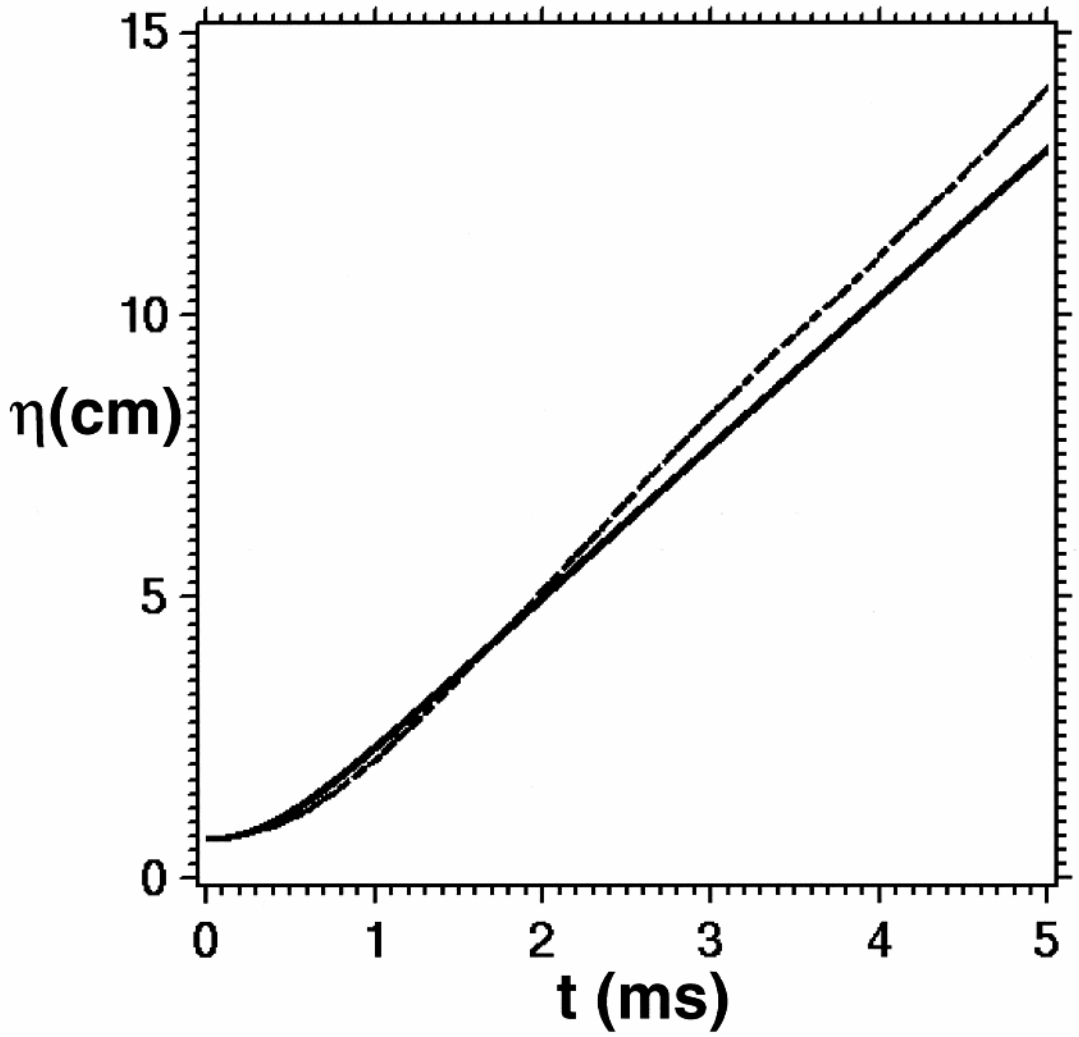

Fig. 6

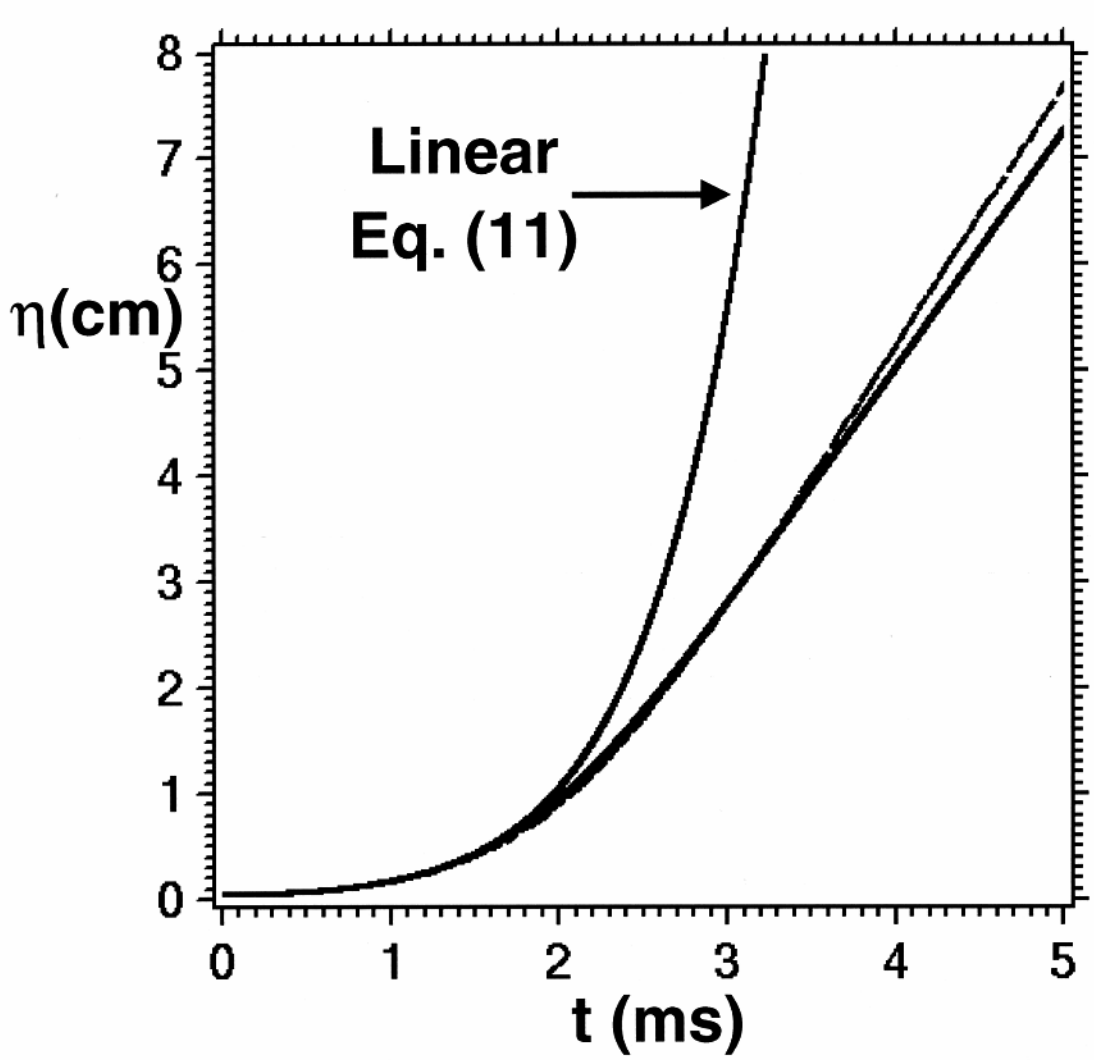

Fig. 7

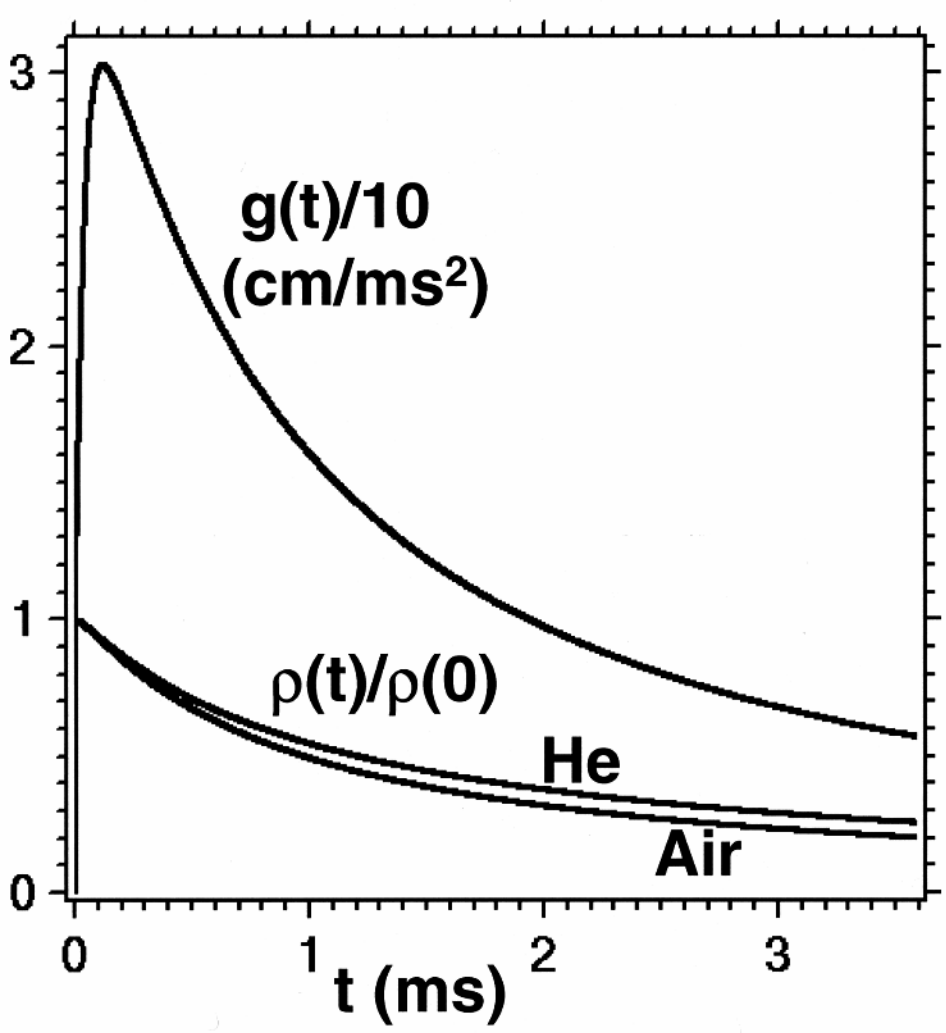

Fig. 8

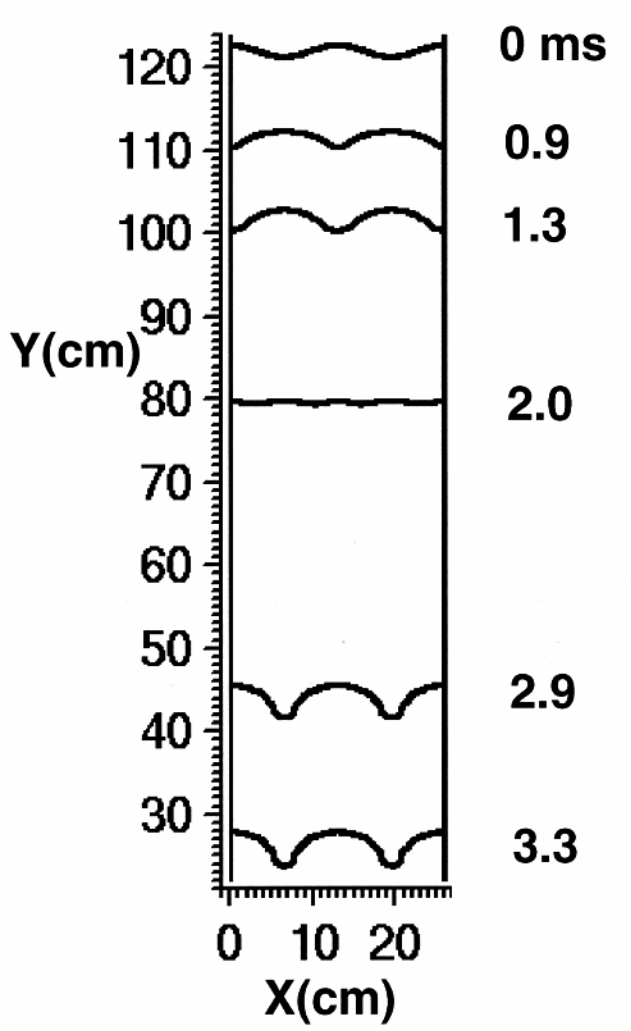

Fig. 9

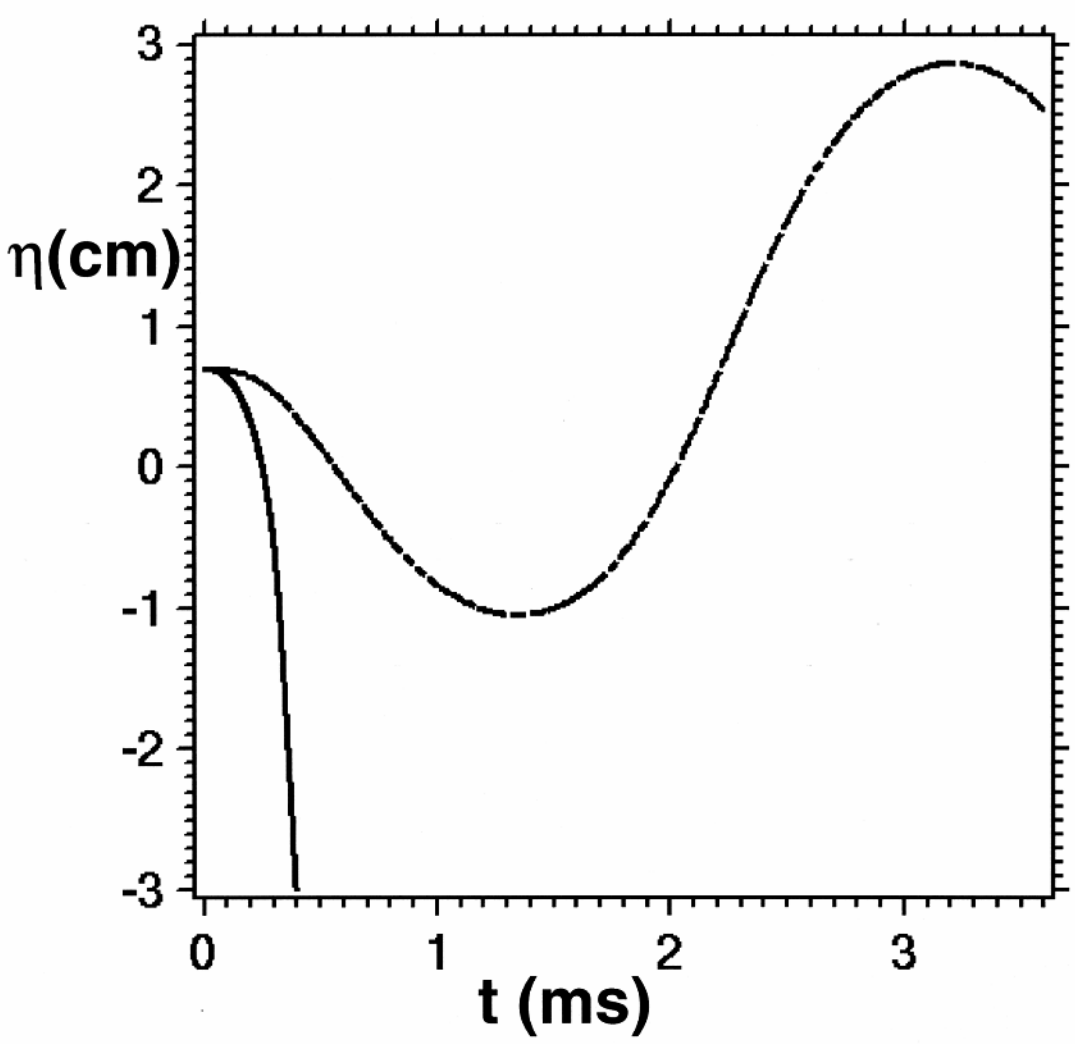

Fig. 10

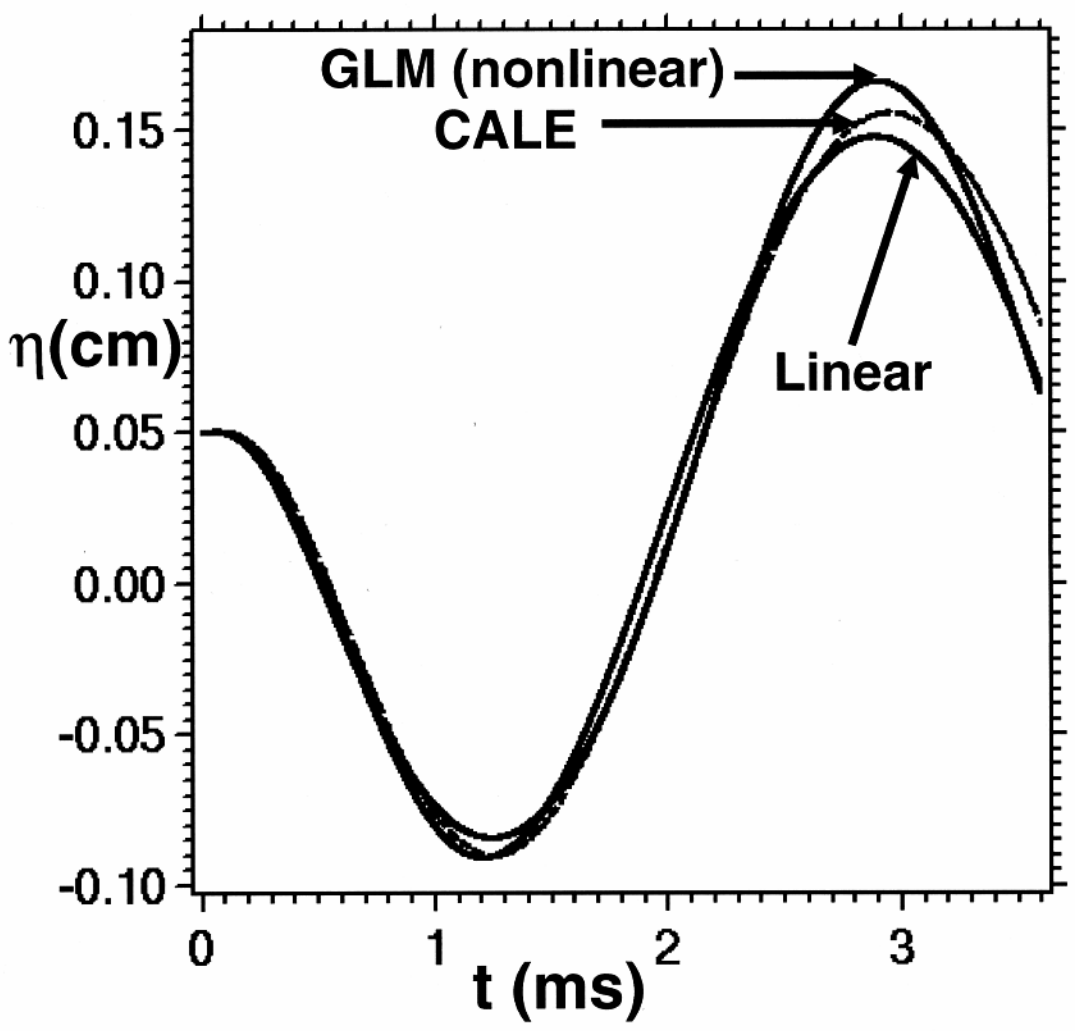
GLM (nonlinear)
CALE
Linear
0.15
0.10
η(cm)
0.05
0.00
-0.05
-0.10
0
1
2
3
t (ms)

Fig. 11

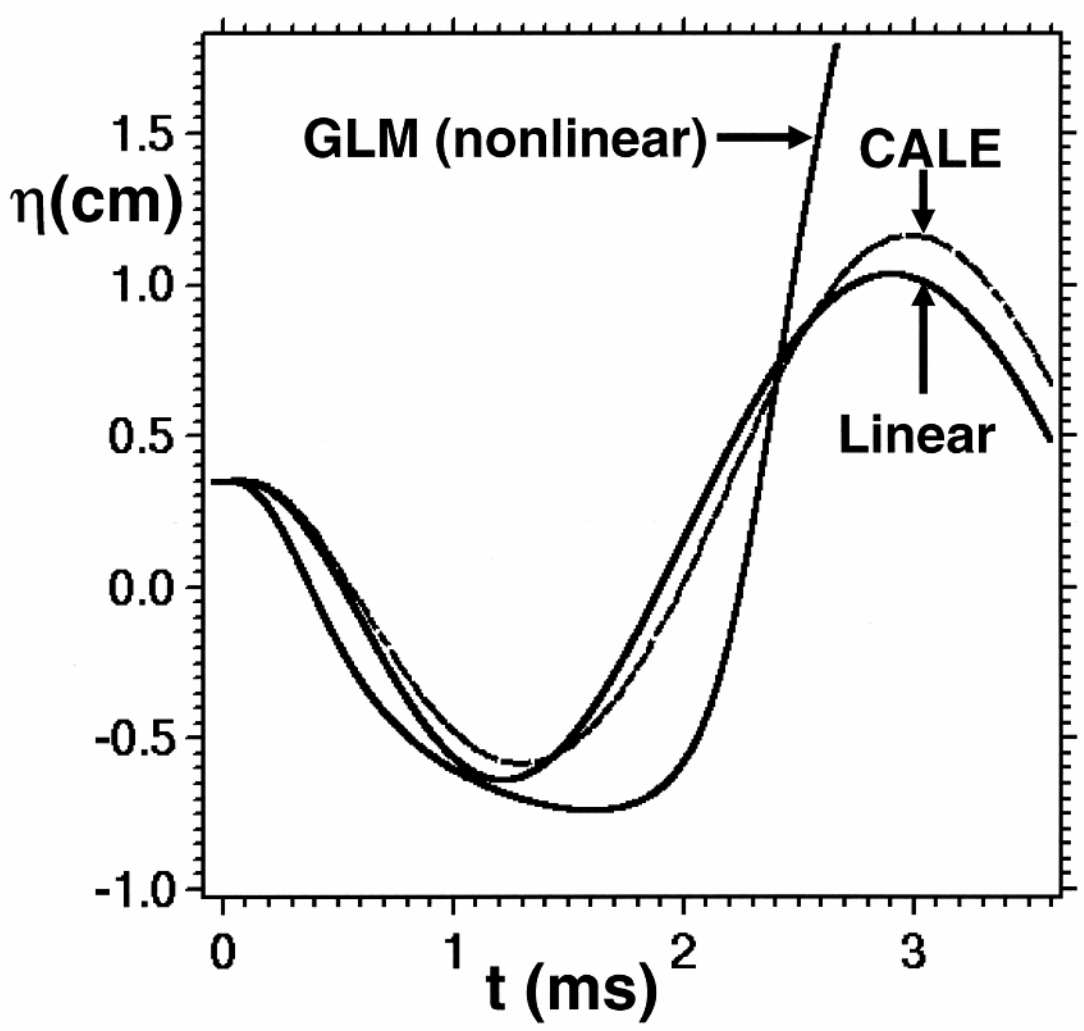

Fig. 12

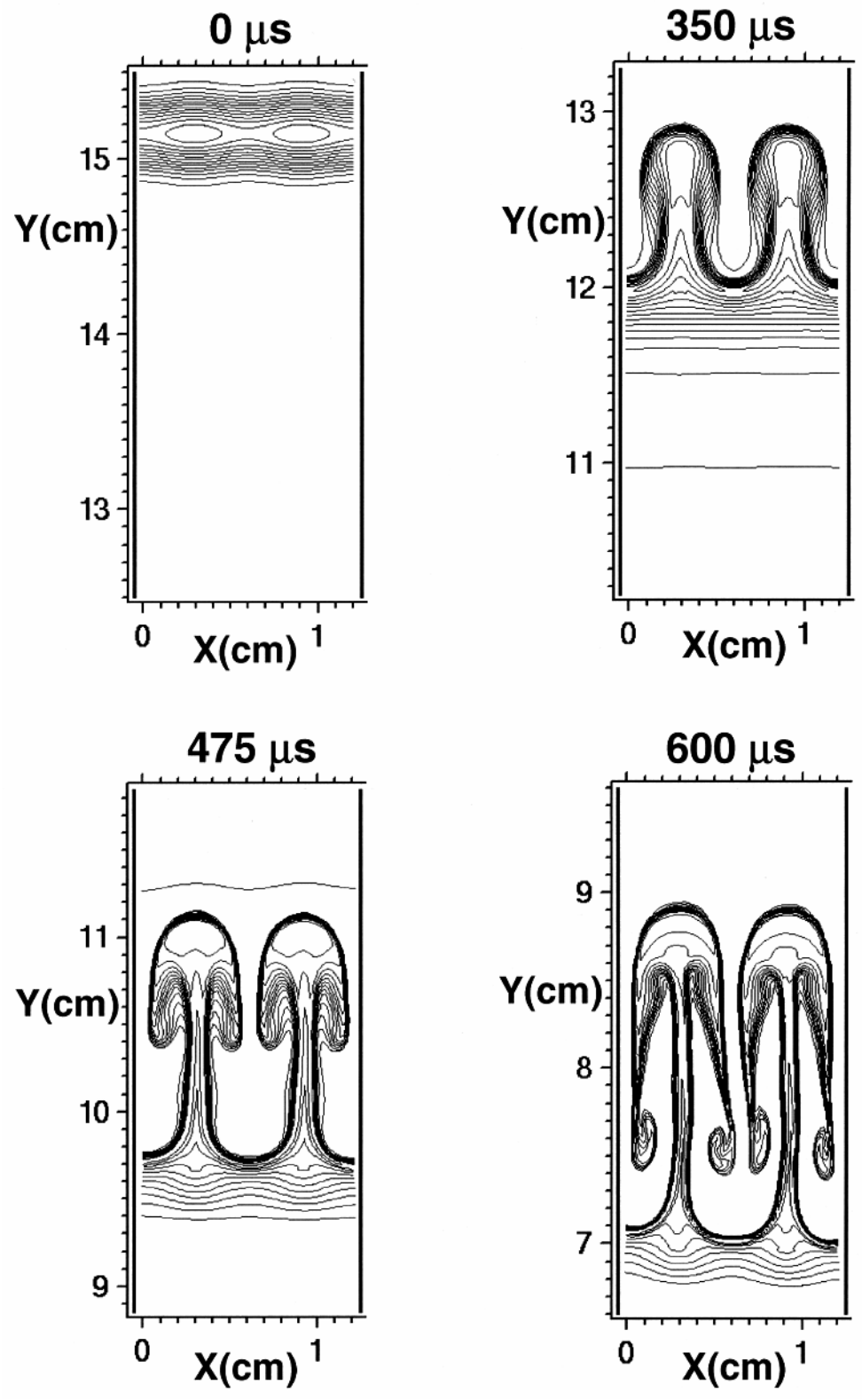
0 μs
15
Y(cm)
14
13
0
X(cm)
1
350 μs
13
Y(cm)
12
11
0
X(cm)
1
475 μs
11
Y(cm)
10
9
0
X(cm)
1
600 μs
9
Y(cm)
8
7
0
X(cm)
1

Fig. 13

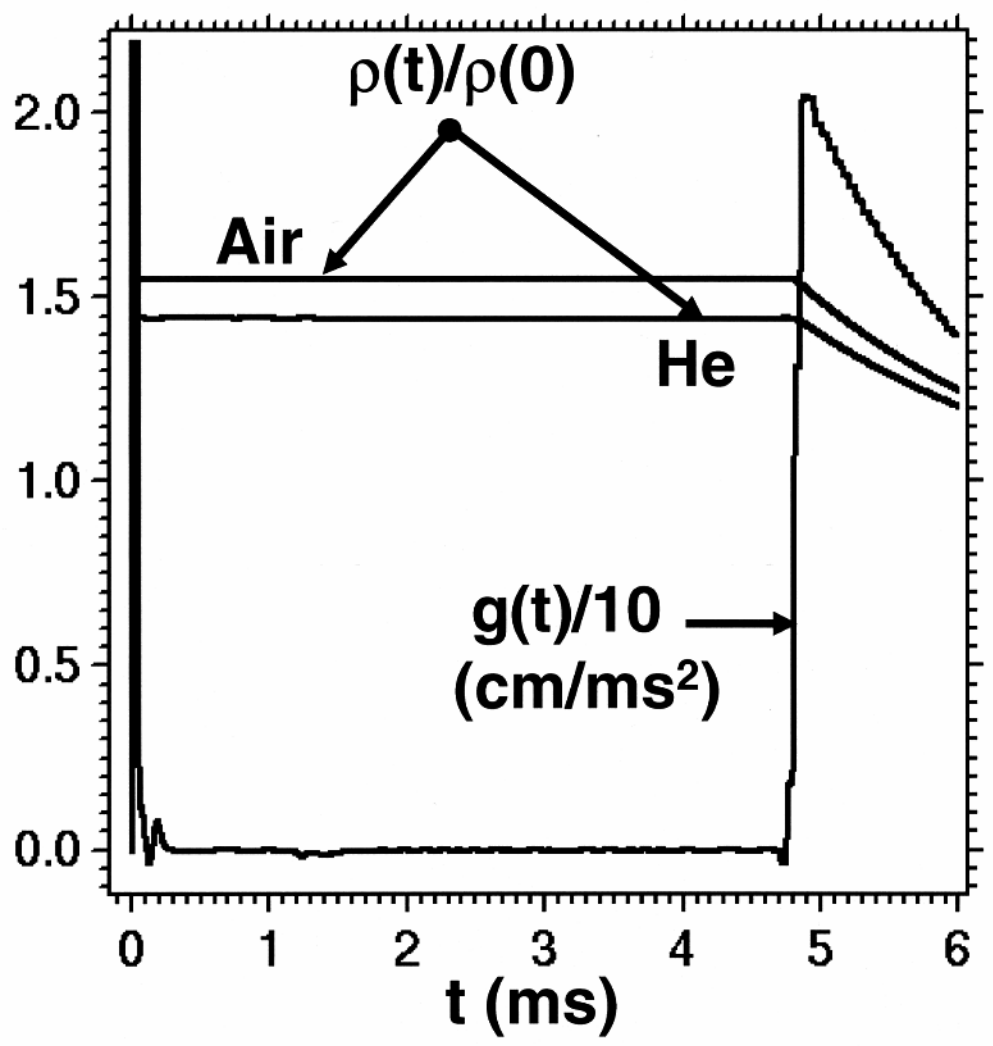

Fig. 14

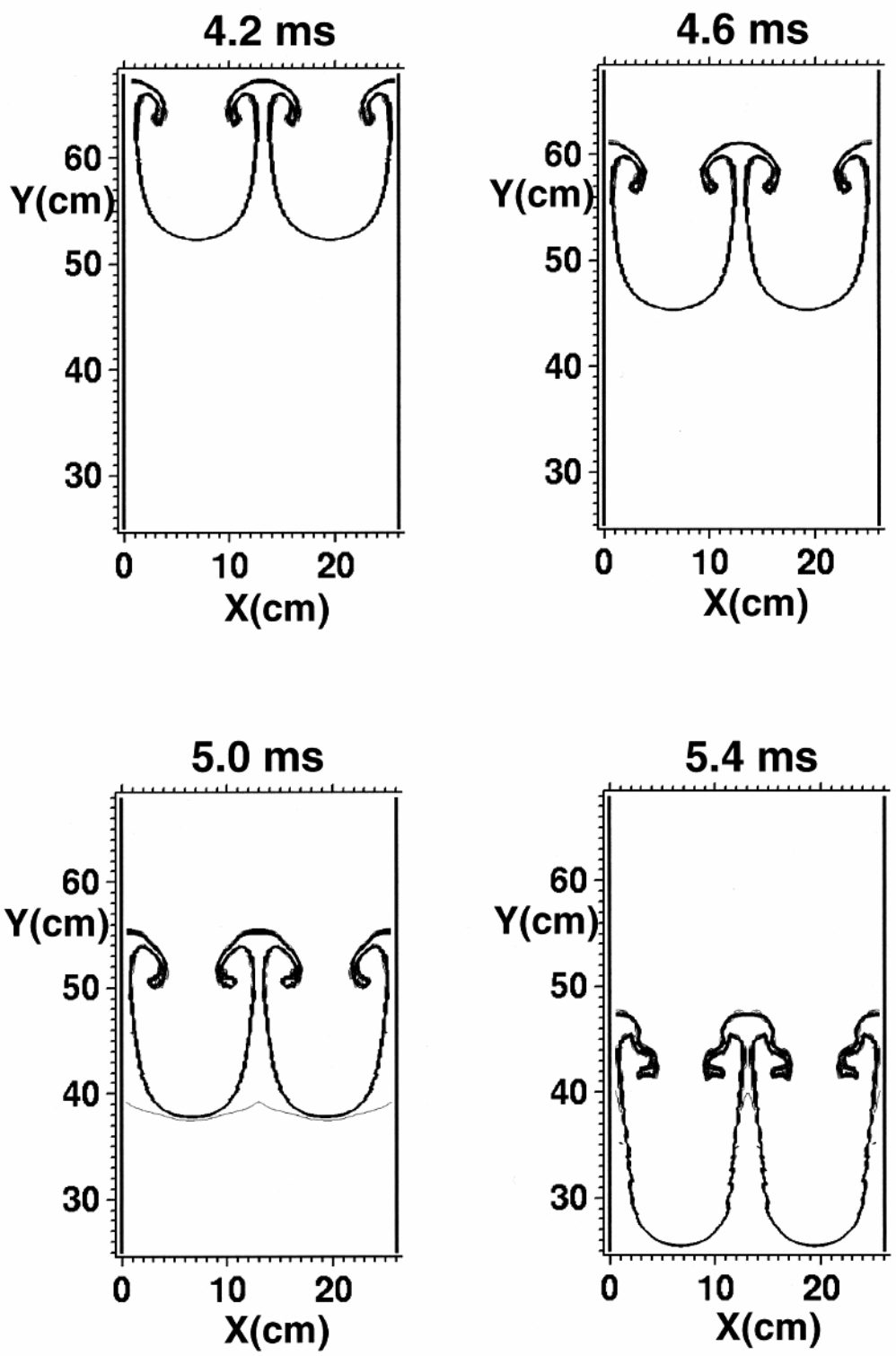

Fig. 15

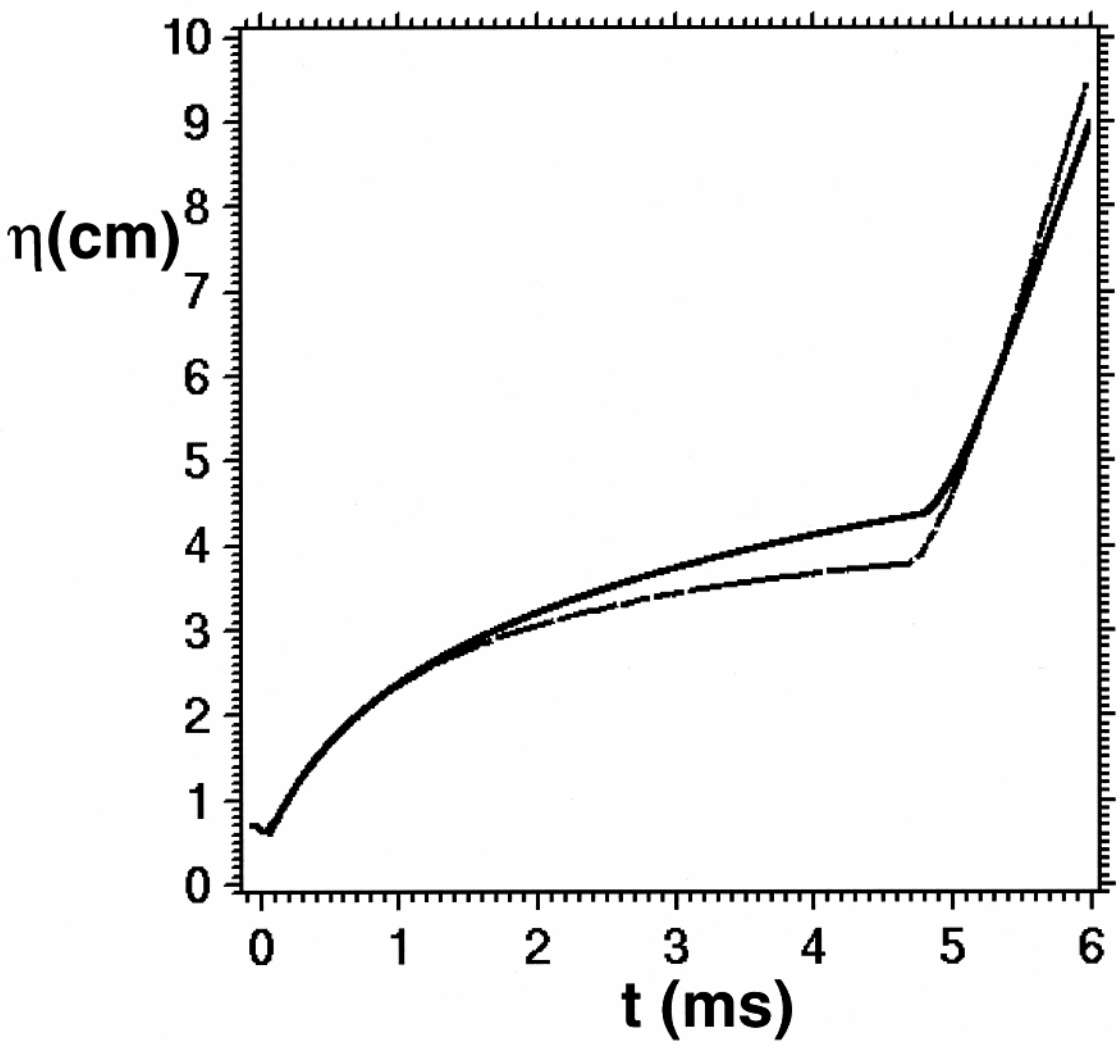

Fig. 16

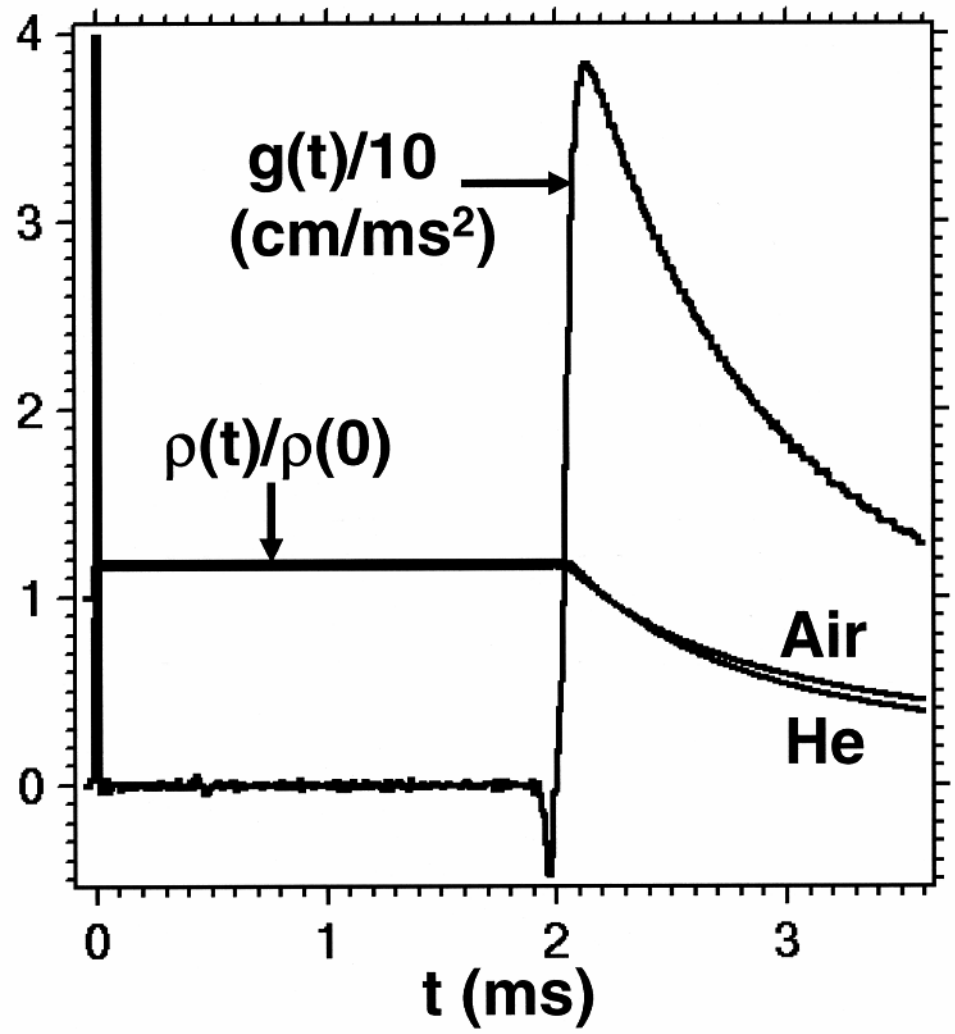

Fig. 17

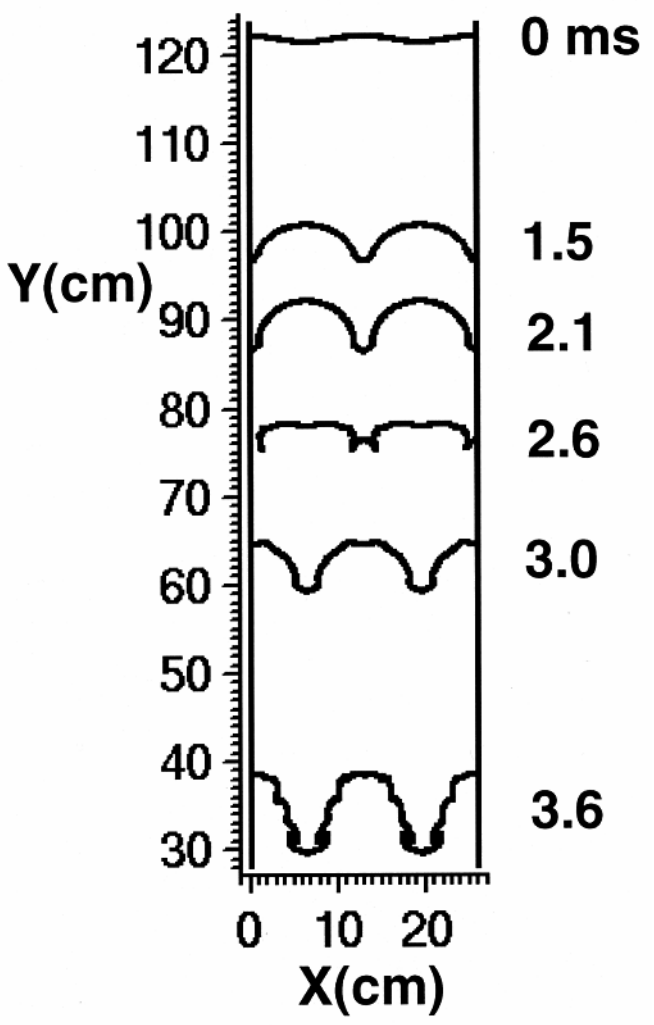

Fig. 18

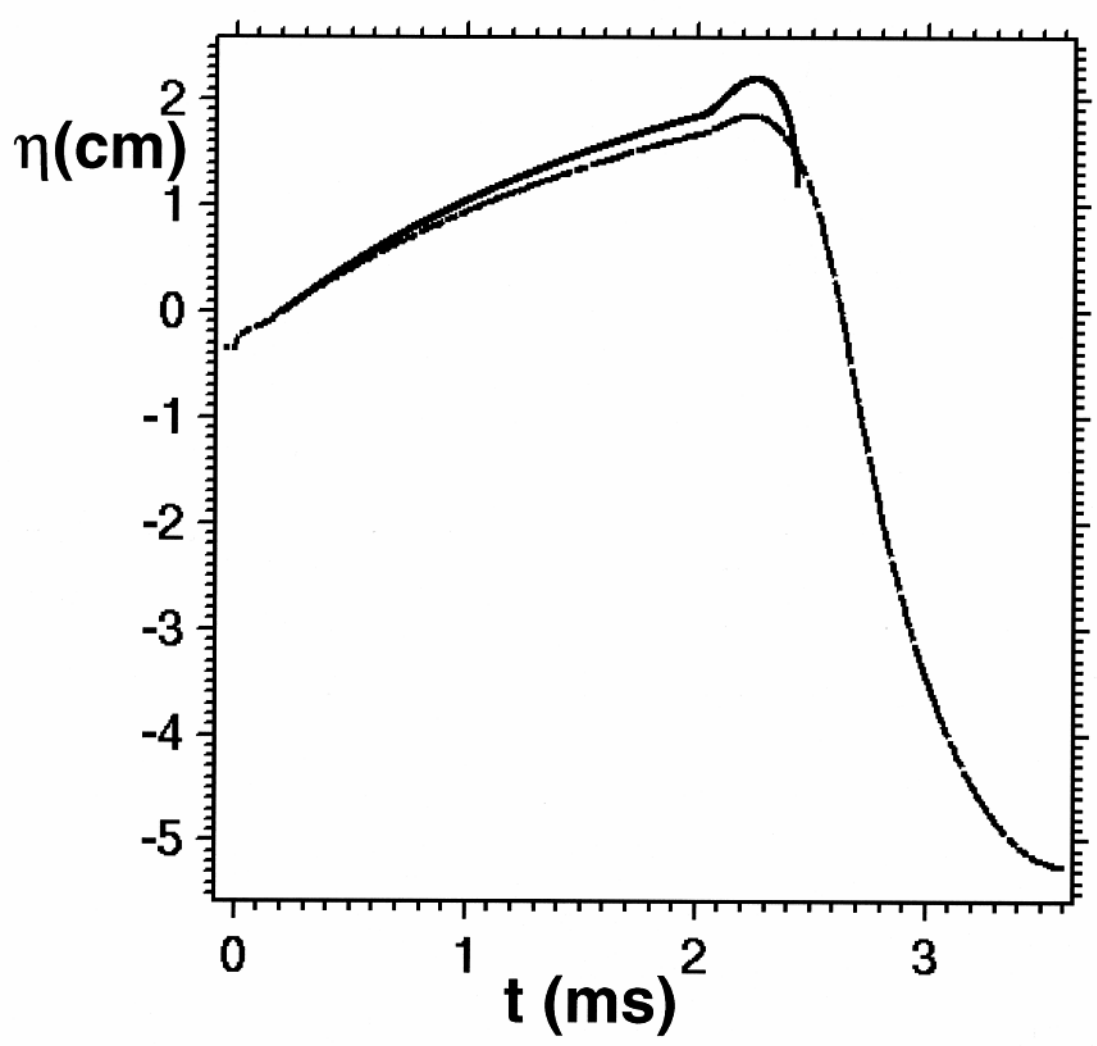

Fig. 19

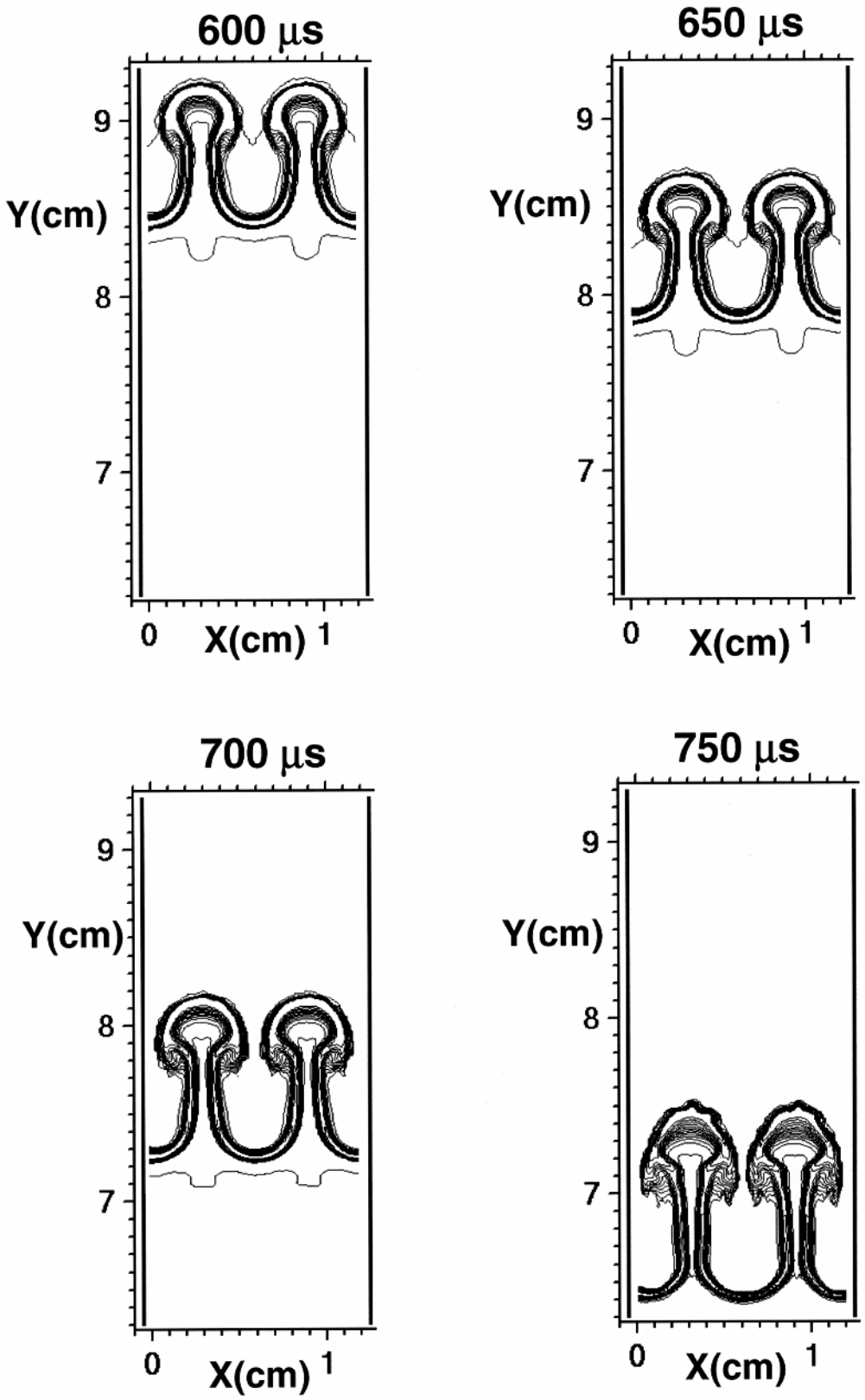

Fig. 20

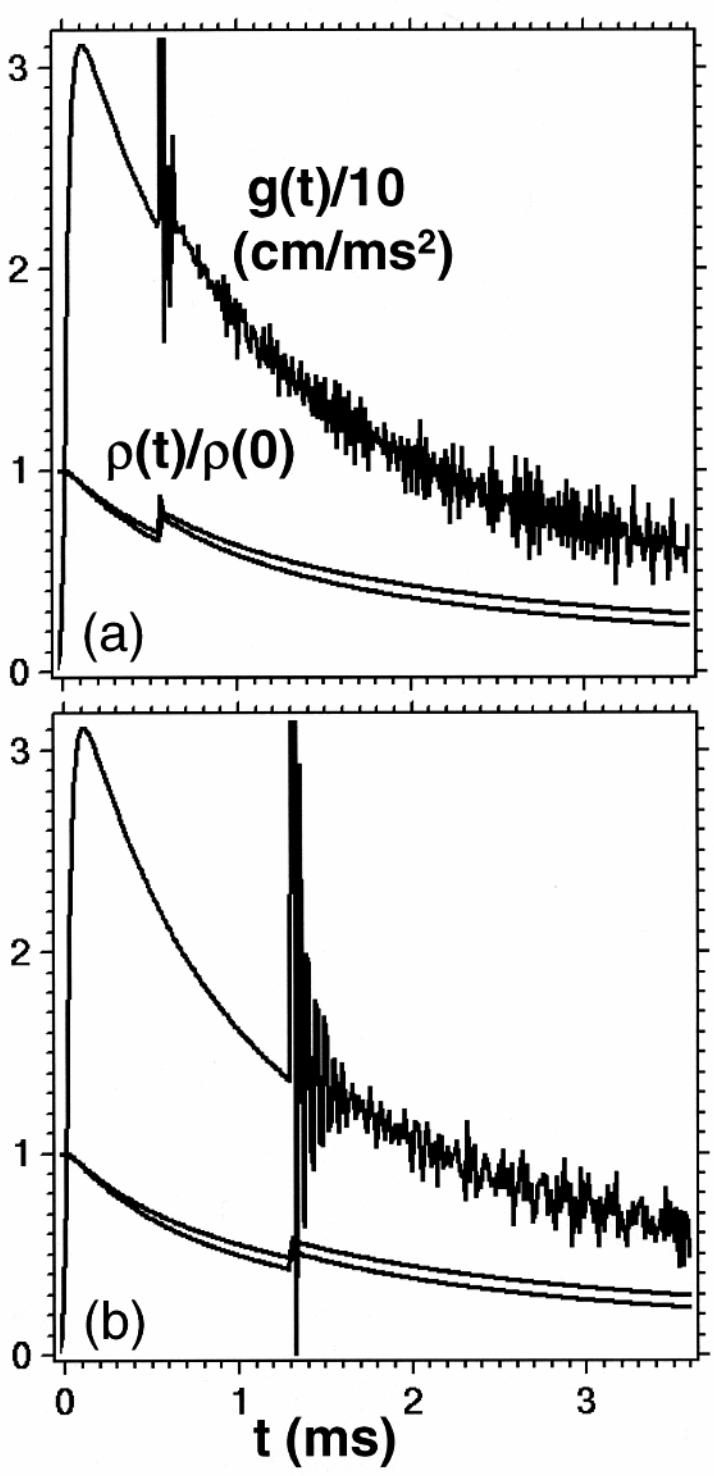

Fig. 21

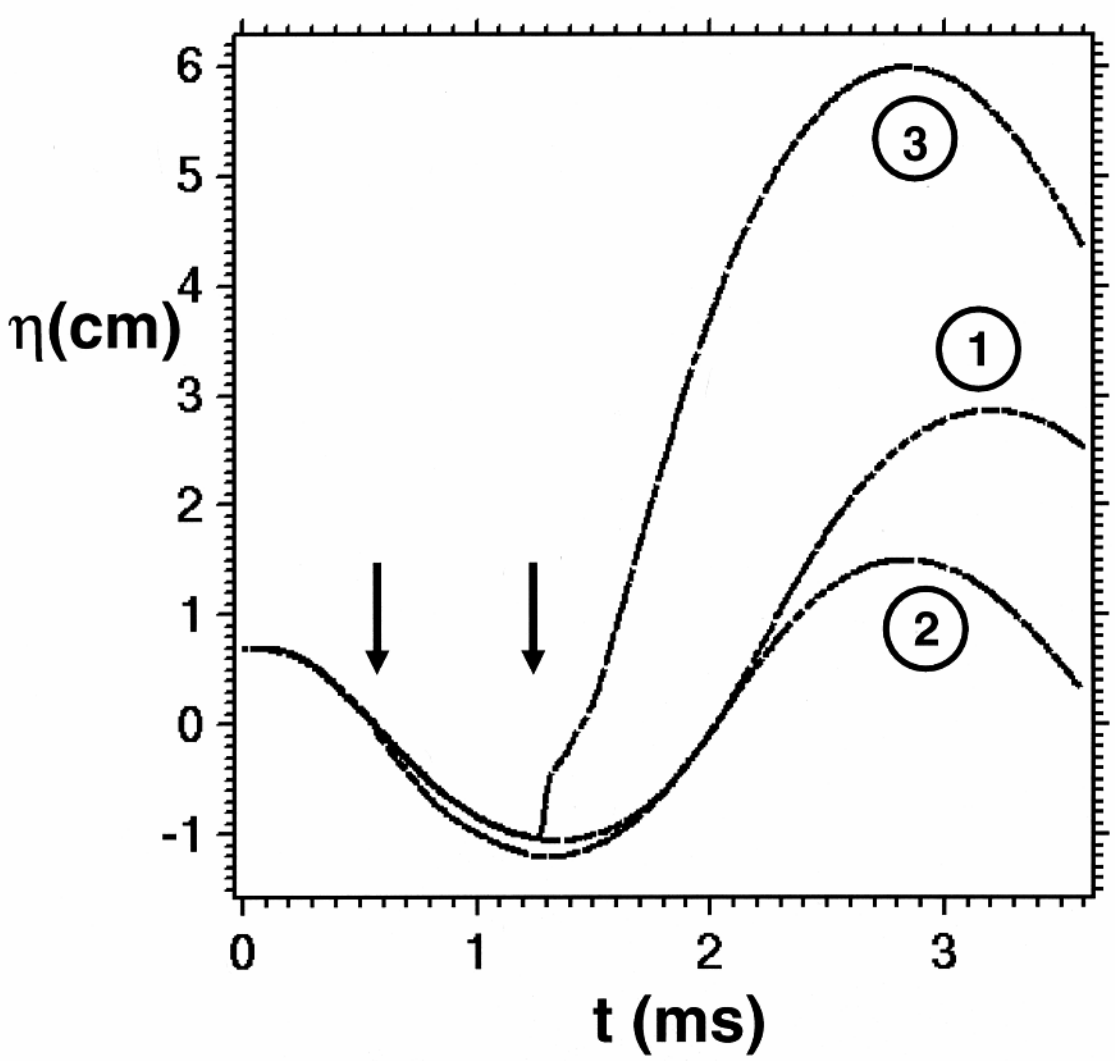

Fig. 22

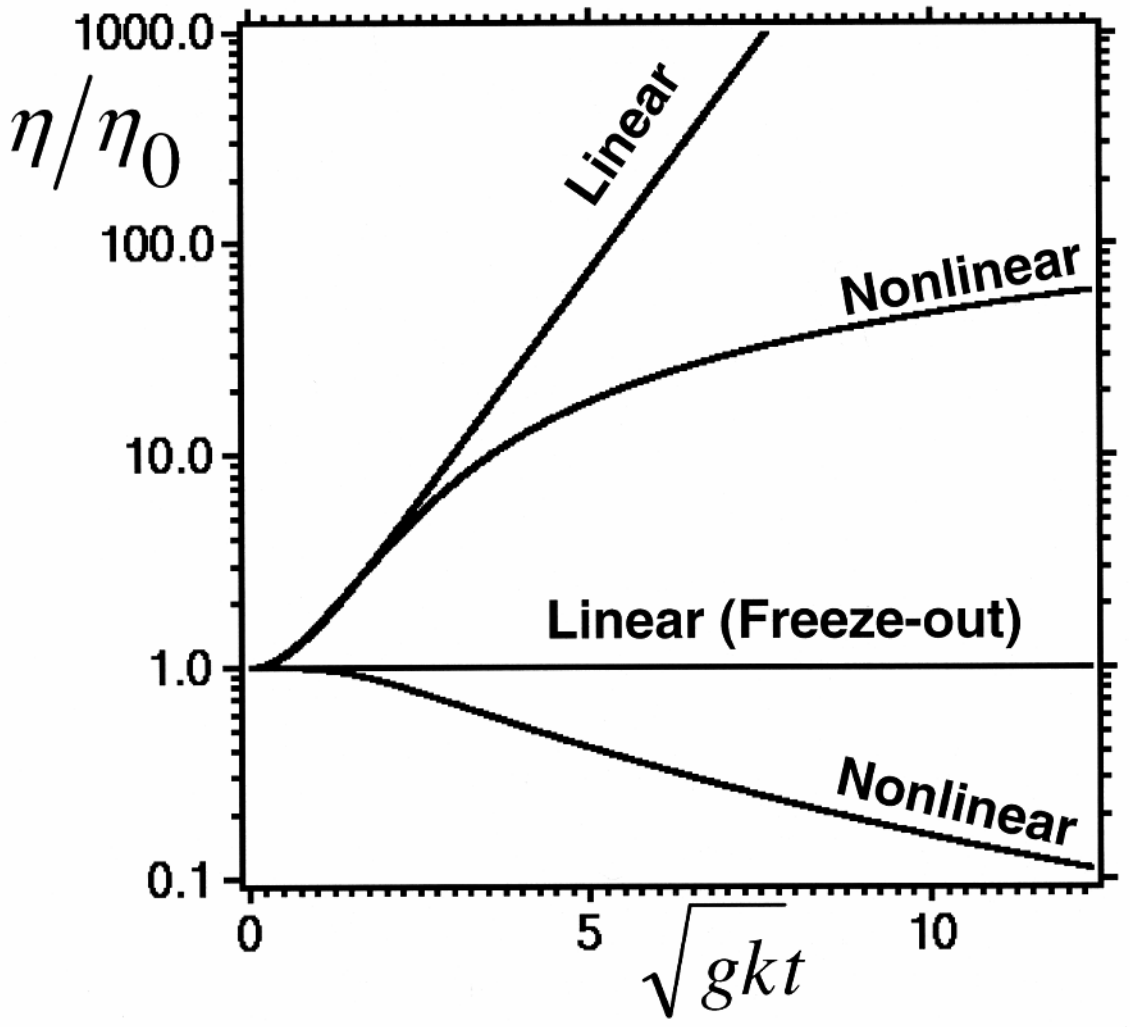
1000.0
100.0
10.0
1.0
0.1
η/η_0
Linear
Nonlinear
Linear (Freeze-out)
Nonlinear
0
5
10
$\sqrt{gkt}$

Fig. 23

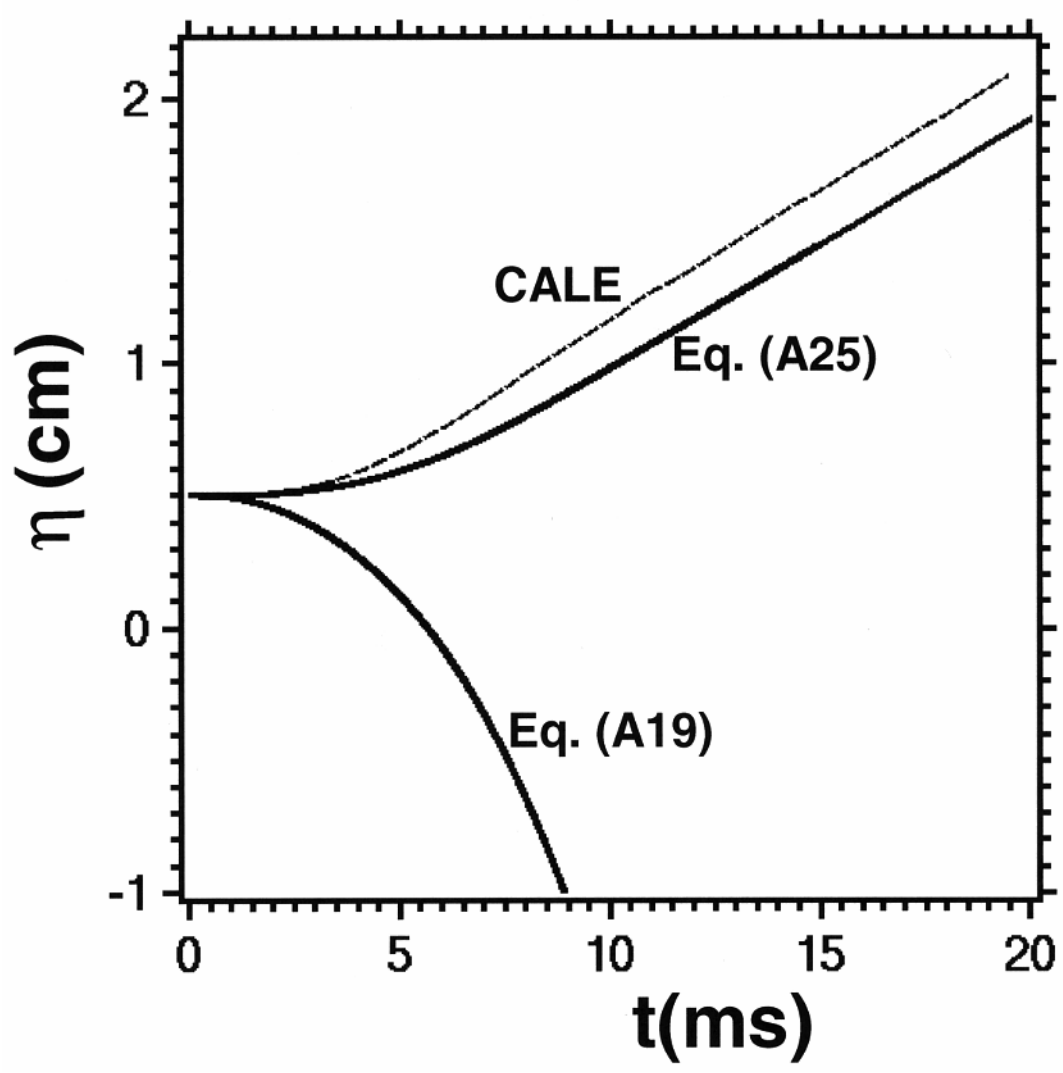

Fig. 24